Editors' Suggestion

Quantum transport in coupled Majorana box systems

Matthias Gau, Stephan Plugge, and Reinhold Egger
Institut für Theoretische Physik, Heinrich-Heine-Universität, D-40225 Düsseldorf, Germany

(Received 7 March 2018; published 16 May 2018)

We present a theoretical analysis of low-energy quantum transport in coupled Majorana box devices. A single Majorana box represents a Coulomb-blockaded mesoscopic superconductor proximitizing two or more long topological nanowires. The box thus harbors at least four Majorana zero modes (MZMs). Setups with several Majorana boxes, where MZMs on different boxes are tunnel coupled via short nanowire segments, are key ingredients to recent Majorana qubit and code network proposals. We construct and study the low-energy theory for multiterminal junctions with normal leads connected to the coupled box device by lead-MZM tunnel contacts. Transport experiments in such setups can test the nonlocality of Majorana-based systems and the integrity of the underlying Majorana qubits. For a single box, we recover the previously described topological Kondo effect which can be captured by a purely bosonic theory. For several coupled boxes, however, nonconserved local fermion parities require the inclusion of additional local sets of Pauli operators. We present a renormalization group analysis and develop a nonperturbative strong-coupling approach to quantum transport in such systems. Our findings are illustrated for several examples, including a loop qubit device and different two-box setups.

DOI: 10.1103/PhysRevB.97.184506

I. INTRODUCTION

Topological superconductors harboring spatially localized Majorana bound states (MBSs) continue to attract a lot of interest; for reviews, see Refs. [1–5]. When different MBSs are located sufficiently far away from each other, they represent fractionalized zero-energy modes: A pair of Majorana zero modes (MZMs) is equivalent to a single fermionic zero mode. Apart from the fundamental interest in experimental observations of such exotic excitations, the potential availability of systems with robust MZMs holds significant promise for applications in topological quantum information processing [6–21]. It is therefore quite exciting that experiments have already provided evidence for MBSs in hybrid superconductor-semiconductor nanowire platforms [22–39] as well as in other material classes [40–44].

A particularly attractive candidate for realizing a MZM-based qubit results from mesoscopic superconducting islands containing four (or more) MZMs. For such a floating island, termed Majorana box (or simply box) in what follows, the Coulomb charging energy E_C plays a dominant role and has to be carefully taken into account [45–48]. Under Coulomb valley conditions, the charge on the island is quantized and the box ground state conserves fermion parity. For a box with four MZMs, one then encounters a twofold degenerate ground state which is equivalent to an effective spin-$1/2$ degree of freedom (qubit) nonlocally built from Majorana states [18]. By arranging tunnel-coupled Majorana boxes in extended two-dimensional (2D) network structures, one obtains topologically ordered phases such as the toric code [9,13,49–51]. Such phases could be useful for quantum information processing applications, e.g., to implement a Majorana surface code [9,13,14]. We note that recent work has also discussed a parafermionic generalization of the Majorana box [52].

On the other hand, for just a single Majorana box, the spin-$1/2$ degree of freedom encoded by the MZMs will be subject to Kondo screening processes if at least three normal leads are connected to the box by tunnel couplings [53–69]. Recalling that Majorana states have a well-defined spin polarization direction [4], for the case of pointlike tunnel contacts, the leads can be modeled as effectively spinless one-dimensional (1D) noninteracting electrons [1]. (We note that Coulomb interactions in the leads have been studied in this context [54,55], but we will not address such effects here.) The exchange couplings of the standard Kondo problem [70,71] are now generated from cotunneling processes connecting different leads through the box, where the lead index takes over the role of the spin up/down quantum number. At low energy scales, such screening processes drive the system towards a stable non-Fermi-liquid fixed point of overscreened multichannel Kondo character, the topological Kondo point [53]. From the viewpoint of multiterminal junction theory [72,73], it is remarkable that this topological Kondo effect (TKE) admits a purely bosonic description via Abelian bosonization for the 1D leads [54,55]. In fact, the physics is then equivalent to the quantum Brownian motion of a particle in a periodic 2D lattice potential which in turn admits an exact solution at very low energies [74,75].

The main goal of this paper is to explore the intermediate situation between just a single box connected to leads (i.e., the single-impurity TKE) and an extended 2D coupled-box network. For instance, consider two Majorana boxes connected by tunnel links, where each box in turn is coupled to at least three normal leads. Such a setup can be viewed as a topological Kondo variant of the celebrated two-impurity Kondo problem [76–78]. In the latter, one encounters a non-Fermi-liquid fixed point not present in the single-impurity Kondo problem. In particular, the fractional quasiparticle charge for the single-impurity topological Kondo problem, which could be probed

2469-9950/2018/97(18)/184506(23) ©2018 American Physical Society

by shot noise [56,67] or via the Josephson effect [65], could now have a different value for the two-impurity setup. With predictions for transport properties of a coupled box device at hand, measurements of the conductance between a given pair of leads, e.g., as a function of temperature or bias voltage, can then yield precious insights about nonlocality effects due to MZMs. Most importantly, by decoupling (or adding) another lead distinct from the pair of leads defining the conductance measurement, one expects a drastic effect on the conductance value [53,56]. Transport measurements could thereby establish that Majorana physics really is behind the device functionality.

In order to address transport and Kondo physics in coupled Majorana box devices in a comprehensive way, we start in Sec. II by describing a theoretical framework suitable for tackling such problems. In particular, we show that Abelian bosonization [70] in combination with the Klein-Majorana fusion approach of Refs. [54,55] allows for a highly versatile formulation of the theory. In Sec. III, we present a detailed study of the weak-coupling regime by means of a one-loop renormalization group (RG) analysis. Loosely speaking, the weak-coupling regime is realized at energies above a suitably defined Kondo scale. We find that the system generally flows towards strong coupling, where in marked contrast to the single-impurity TKE [54,55], an effectively bosonic description no longer applies. In general, one has to take into account additional nonconserved local fermion parities which can be represented by sets of Pauli operators. Such spinlike variables are shown to play a crucial role for an understanding of transport in basically all coupled Majorana box devices. In Sec. III, we also provide an explicit RG analysis for three device examples of current experimental interest, including the 'loop qubit' device proposed in Ref. [19]. Next, in Sec. IV, we turn towards the strong-coupling regime approached at very low energy scales. By focusing on the most relevant degrees of freedom, which can be identified from the weak-coupling RG flow and by employing quantum Brownian motion arguments [74,75], we derive and study the effective low-energy theory corresponding to this regime. Employing also Emery-Kivelson-type transformations [70,79–83], Sec. IV provides a nonperturbative strong-coupling analysis for all three examples studied in Sec. III from the weak-coupling perspective. In Sec. V, we present the exact solution for quantum transport in a simple two-box device at a Toulouse point which exhibits two-channel Kondo physics. Finally, we offer some conclusions in Sec. VI. Technical details have been delegated to several appendices, and we put $\hbar = k_B = 1$ and the density of states in the leads $\nu = 1$ throughout.

In most chapters below, we include general sections introducing broadly applicable concepts and ideas of how to tackle transport in coupled Majorana boxes, followed by select simple examples that are of current interest. To follow the general discussion, the interested reader may find it useful to seek clarity about concrete applications in one or two of these examples and to revisit the general discussion once those are understood.

II. MODEL AND LOW-ENERGY APPROACH

The central goal of this paper is to understand the low-energy physics of multiterminal junctions defined by a set of noninteracting normal-conducting leads with pointlike tunnel contacts to a general coupled Majorana box device. A concrete example for such a setup is shown in Fig. 1. We start in Sec. II A by describing the basic model employed here and the physical assumptions behind it. For pointlike lead-MBS tunnel contacts, it is well known that noninteracting leads can be modeled as effectively 1D spinless leads [1,70,71]. Subsequently, in Sec. II B we express these 1D lead fermions in terms of Abelian bosonization [70], which offers a convenient route to access the important low-energy modes. Tunneling processes are then analyzed in Sec. II C. Finally, in Sec. II D, we focus on Coulomb valley conditions and describe the effective low-energy theory projected to the charge ground state of each Majorana box in the system.

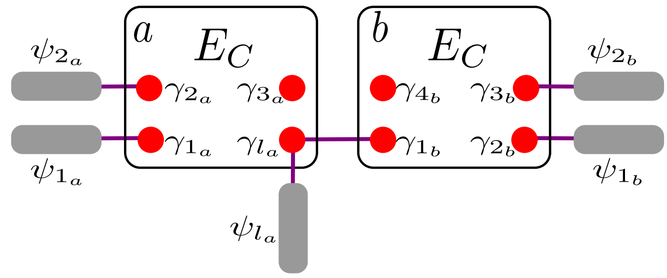

FIG. 1. Example for a device with two Majorana boxes (a,b) connected by a single tunnel bridge (violet). Each box is subject to a charging energy E_C and hosts four MZMs with corresponding Majorana operators $\gamma_{j_{a/b}}$ (filled red circles). Both boxes are connected to several normal leads, with corresponding fermion operators $\psi_{j_{a/b}}(x)$ (indicated in gray), via lead-MZM tunnel links (violet). For box a/b, we have $M_{a/b}$ simple lead-MZM tunnel contacts. Simple contacts are characterized by an only pairwise coupling between a lead fermion operator $\Psi_{j_a} = \psi_{j_a}(0)$ and a MZM operator γ_{k_a}, see Eq. (3), without couplings to other leads or MZMs. For the shown case with $M_a = M_b = 2$, the only nonsimple contact corresponds to lead fermion ψ_{l_a}.

A. Model

Let us start with the description of a single Majorana box, which for the moment is assumed decoupled from all other boxes and from all leads. For concrete layout proposals, see Refs. [18,19]. Following the discussion in Refs. [53–56], on energy scales well below the proximity-induced topological superconducting gap Δ, we can neglect above-gap quasiparticle excitations. In addition, throughout this paper, we will assume that all MBSs on a given box are located far away from each other and therefore can be viewed as MZMs. (For a discussion of hybridization effects between MBSs on a given box, see Ref. [57].) Under these conditions, we only need to take into account Cooper pairs and MZMs, where Majorana operators are self-adjoint, $\gamma_j = \gamma_j^\dagger$, and obey the Clifford algebra $\{\gamma_j,\gamma_k\} = 2\delta_{jk}$ [1–5]. We now take into account the box charging energy E_C, where $E_C \approx 1$ meV for typical experimental realizations [29]. This energy scale plays a central role for all coupled box devices studied below. In particular, it facilitates phase-coherent electron transport, which in turn generates nontrivial correlations between different boxes and/or leads. This basic mechanism is also behind many recently proposed quantum information processing schemes for Majorana qubits and Majorana code networks [13–21].

Under the above conditions, the Hamiltonian of an isolated box is solely due to Coulomb charging,

$$H_{\text{box}} = E_C(\hat{Q} - n_g)^2, \tag{1}$$

where the dimensionless parameter n_g is controlled by backgate voltages. We assume the same value of E_C for all boxes below since different charging energies do not cause qualitative changes as long as they remain sufficiently large. The operator $\hat{Q}$ has integer eigenvalues Q and describes the total charge on the box in units of the elementary charge e. In general, $\hat{Q}$ receives contributions both from Cooper pairs and from the MZM sector. However, it is most convenient to adopt a gauge where the Majorana operators do not carry charge but instead are accompanied by $e^{\pm i\varphi}$ operators whenever the box charge changes by one unit, $Q \to Q \pm 1$ [45]. By this choice, φ is the phase operator conjugate to $\hat{Q}$, i.e., $[\varphi,\hat{Q}] = i$. For each Majorana box, the charge dynamics is therefore captured by a dual pair of local bosonic fields. For illustrative purposes, we consider boxes harboring four MZMs below. The generalization of our approach to an arbitrary even number of MZMs for a given box is straightforward.

Next we include the effects of a single MZM-MZM tunnel link connecting two Majorana boxes a/b, cf. Fig. 1, via the tunneling Hamiltonian [45,46]

$$H_t = t_{j_a k_b}\gamma_{j_a}\gamma_{k_b}e^{i(\varphi_a-\varphi_b)} + \text{H.c.} \tag{2}$$

with the MZM operators γ_{j_a} and γ_{k_b}. The index j_a (k_b) here means that we label MZMs belonging to box a (b), cf. Fig. 1, and the $e^{\pm i\varphi_{a,b}}$ operators describe the transfer of charge in a tunneling event. Physically, the $e^{i(\varphi_a-\varphi_b)}$ factor in Eq. (2) amounts to the formation of a charge dipole between both boxes. Finally, $t_{j_a k_b}$ is a microscopic tunnel amplitude connecting the respective MZMs, e.g., through an intermediate nontopological nanowire segment.

For pointlike lead-MZM tunnel contacts, we can now describe each noninteracting lead by a 1D spinless fermion operator $\psi_{j_a,R/L}(x)$ [1,70,71], where the index j_a indicates that the lead is tunnel coupled to box a. Choosing $x = 0$ as the tunnel-contact point, right- and left-moving (R/L) fermions are defined for $x < 0$, with the open boundary conditions $\psi_{j_a,L}(0) = \psi_{j_a,R}(0)$. By a standard unfolding transformation [70], we may switch to chiral (right-moving) fermions, $\psi_{j_a}(x)$, by writing $\psi_{j_a}(x) = \psi_{j_a,R}(x)$ for $x < 0$ and $\psi_{j_a}(x) = \psi_{j_a,L}(-x)$ for $x > 0$. The lead-MZM contact is then described by the tunneling Hamiltonian

$$H_\lambda = \lambda_{j_a k_a}\Psi^\dagger_{j_a}\gamma_{k_a}e^{-i\varphi_a} + \text{H.c.}, \tag{3}$$

where $\lambda_{j_a k_a}$ again is a microscopic tunneling amplitude and we employ the shorthand notation $\Psi_{j_a} = \psi_{j_a}(0)$.

All tunnel couplings will be assumed so weak that they can neither create above-gap quasiparticle excitations nor destroy the integrity of MBSs. We thus require that the energy scales associated with the amplitudes $t_{j_a k_b}$ and $\lambda_{j_a k_a}$ are small compared to both Δ and E_C. Moreover, we note that physical tunnel contacts extend only over short distances within the coupled box device. The only exception to this rule are long-ranged pairwise cotunneling events generated via charging effects, see Sec. II D below.

Finally, the Hamiltonian of decoupled lead no. j is given by

$$H_{\text{leads}} = -iv_F\int_{-\infty}^{\infty} dx\ \psi_j^\dagger\partial_x\psi_j, \tag{4}$$

where we assume the same Fermi velocity v_F for all leads and write $j = j_a$ for notational simplicity. Differences in Fermi velocities are not important and can be taken into account by renormalizing the above tunneling amplitudes.

B. Abelian bosonization

So far we have considered a fermionic description of the leads. By inspecting the tunneling Hamiltonians (2) and (3), we observe that it will also be useful to switch to a bosonized description for the leads. As for the Majorana box above, fermionic (statistical) and bosonic (charge/phase) lead variables are thereby explicitly separated. While the lead Hamiltonian (4) admits a purely bosonic description, see Eq. (7) below, fermionic aspects do appear in tunneling operators connecting the respective lead to MZMs or to other leads. In terms of right and left movers, Abelian bosonization states the correspondence [70]

$$\psi^\dagger_{j,R/L}(x) = \frac{\kappa_j}{\sqrt{\alpha}}e^{i[\phi_j(x)\pm\theta_j(x)]} \tag{5}$$

with a short-distance cutoff length α. The dual boson fields ϕ_j and θ_j obey the algebra $[\phi_j(x'),\partial_x\theta_k(x)] = i\pi\delta(x-x')\delta_{jk}$, and κ_j denotes a Klein factor ensuring anticommutation relations with all other lead fermions and all MZM operators. Following Refs. [54,55], we use a Majorana fermion representation for Klein factors, i.e., $\kappa_j^\dagger = \kappa_j$ and $\{\kappa_j,\kappa_k\} = 2\delta_{jk}$. Noting that the open boundary conditions for lead fermions translate to $\theta_j(0) = 0$, and using the shorthand notation

$$\Phi_j = \phi_j(0), \quad \Theta'_j = \partial_x\theta_j(0), \tag{6}$$

the lead fermion operator in Eq. (3) takes the form $\Psi_j^\dagger = \alpha^{-1/2}\kappa_j e^{i\Phi_j}$. Similarly, the electron density operator near the tunnel contact is proportional to Θ'_j.

The lead Hamiltonian (4) is given by [70]

$$H_{\text{leads}} = \frac{v_F}{2\pi}\int_{-\infty}^{0} dx[(\partial_x\phi_j)^2 + (\partial_x\theta_j)^2]. \tag{7}$$

For a description of tunneling processes, however, Klein factors play a crucial role. Using bosonized expressions, each tunneling event is factorized into a charge-neutral fermion-bilinear part encoding the fermionic statistics and a part describing the bosonic charge (or phase) dynamics. Explicitly, for the lead-MZM tunneling Hamiltonian in Eq. (3), we obtain

$$H_\lambda = \lambda_{j_a k_a}\kappa_{j_a}\gamma_{k_a}e^{i(\Phi_{j_a}-\varphi_a)} + \text{H.c.}, \tag{8}$$

where a factor $1/\sqrt{\alpha}$ has been absorbed in $\lambda_{j_a k_a}$. We notice that Eq. (8) contains a local fermion parity operator $i\kappa_{j_a}\gamma_{k_a}$ with eigenvalues ± 1 corresponding to the occupation number of the fermion mode built from κ_{j_a} and γ_{k_a}.

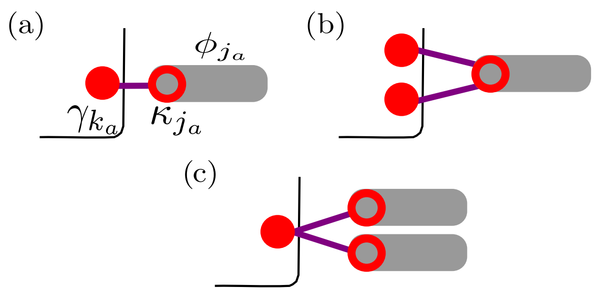

FIG. 2. Simple vs nonsimple lead-MZM tunnel junctions, see Sec. II C. Filled red circles correspond to MZMs γ_{k_a} and open red circles to Klein-Majorana operators κ_{j_a} within a bosonized description of lead fermions, see Eq. (5). (a) Simple contact, cf. Eq. (8). (b) Nonsimple contact between two MZMs and one lead, cf. Eq. (11). (c) Nonsimple contact between one MZM and two leads, cf. Eq. (12).

C. Simple vs nonsimple contacts

It is convenient for the subsequent discussion to introduce the notion of a *simple* lead-MZM contact, and generally that of a simple tunnel junction. For a simple contact, see Fig. 2(a), we require that the tunnel-coupled Majorana (γ_{k_a}) and lead (Ψ_{j_a}) fermions have no additional tunnel couplings to other (Majorana or lead) fermions. All lead-MZM junctions beyond the pairwise tunnel contact in Fig. 2(a) are referred to as *nonsimple*. Two examples of such nonsimple lead-MZM contacts are shown in Figs. 2(b) and 2(c), see also Ref. [84]. A nonsimple junction also occurs when a lead-contacted MZM is in addition tunnel coupled to another MZM on an adjacent box, see Fig. 1. Similarly one may refer to nonsimple MZM-MZM junctions if several MZMs on distinct boxes are coupled to each other.

For systems with only simple contacts, we can then proceed in a straightforward manner by employing the Klein-Majorana fusion approach put forward in Refs. [54,55]. To that end, we observe that in such systems, each local fermion parity built from a Klein-Majorana operator κ_{j_a} and a MZM operator γ_{k_a} forming the respective tunnel contact, cf. Fig. 2(a), will be separately conserved, $i\kappa_{j_a}\gamma_{k_a} = \pm 1$. Similarly, all local parities associated with MZM-MZM tunnel links are conserved, $i\gamma_{j_a}\gamma_{k_b} = \pm 1$. The above observations imply that the fermionic sector of the theory is trivially solvable so long as all local fermion parities remain conserved. A coupled Majorana box system with only simple contacts can thus be reduced to a purely bosonic theory, which is generally much simpler to analyze than the original fermionic version.

In this paper, we address situations where some of the above local fermion parities are not conserved anymore. This may happen if unintentional parity-breaking mechanisms are present, e.g., when a conventional midgap Andreev state is accidentally centered near a lead-contacted MBS and thereby activates quasiparticle poisoning mechanisms [63]. We instead will focus on intentional parity-breaking effects due to nonsimple tunnel contacts. Such cases pertain to many Majorana box transport setups and quantum-information processing applications. In fact, local parity conservation implies that for systems with only simple contacts, MZMs cannot reveal their underlying fermionic statistics since different measurement bases are not accessible. With the above motivation, we now inspect several generic scenarios.

1. Charge degenerate boxes

Our first example for parity-breaking mechanisms is tied to fluctuating charge states on a given box, e.g., because the gate parameter n_g in Eq. (1) is tuned close to a half-integer value. This case has also been studied in the context of the single-impurity TKE [64,68,69]. In general, a large box charging energy E_C will admit at most a few low-energy charge states. As a consequence, charging effects also constrain the box fermion parity which can be written as the product of MZM operators on the box. For the four-MZM box [53], we have $\mathcal{P}_{\rm box} = \gamma_1\gamma_2\gamma_3\gamma_4$.

For n_g close to a half-integer value and/or for strong lead-MZM tunnel couplings, the box charge can fluctuate strongly. Retaining only the nearly degenerate lowest-energy charge states $|Q\rangle_a$ and $|Q+1\rangle_a$ on box no. a, where the integer Q is chosen such that $Q < n_g < Q+1$, it is convenient to introduce a corresponding spin-1/2 operator $\mathbf{S}_a$. With $S_{\pm,a} = S_{x,a} \pm iS_{y,a}$, it has the components [45]

$$S_{z,a} = (|Q+1\rangle_a - |Q\rangle_a)/2,$$
$$S_{+,a} = S^\dagger_{-,a} = e^{i\varphi_a} = |Q+1\rangle_a \langle Q|_a . \qquad (9)$$

Projecting Eqs. (1), (2), and (8) to the Hilbert subspace spanned by $|Q\rangle_a$ and $|Q+1\rangle_a$, the Hamiltonian schematically takes the form [64,69]

$$H_{\rm deg} = \Delta E_a S_{z,a} + \sum_{j_a,k_b} \left(t_{j_a k_b}\gamma_{j_a}\gamma_{k_b} S_{+,a} e^{-i\varphi_b} + \text{H.c.}\right)$$
$$+ \sum_{j_a,k_a} \left(\lambda_{j_a k_a}\gamma_{j_a}\kappa_{k_a} S_{+,a} e^{-i\Phi_{k_a}} + \text{H.c.}\right), \qquad (10)$$

where the energy ΔE_a is controlled by the detuning of n_g away from half integers and we use the definition in Eq. (6). While $H_{\rm deg}$ in Eq. (10) allows $\mathcal{P}_{\rm box}$ to fluctuate, such fluctuations are perfectly correlated with charge hopping processes on and off the box: The MZM operator γ_{j_a} is always accompanied by $S_{\pm,a}$, see Eq. (10). As long as the system only has simple lead-MZM contacts, one therefore arrives at a purely bosonic description again. In fact, while details of the single-impurity TKE such as the value of the Kondo temperature depend on the backgate parameter, the low-energy behavior is basically independent of n_g [64,69]. By implementing an entangled lead-MZM fermion basis, the Klein-Majorana fusion approach is thus highly useful also for charge-degenerate Majorana box devices. We will see that this conclusion applies even in a much wider sense.

2. Nonsimple contacts

Next we consider device layouts with at least one nonsimple contact where in- or out-tunneling of charge from the box can take place either via different MZMs on the box [Fig. 2(b)] or through different leads [Fig. 2(c)]. The presence of such contacts has important consequences on low-energy quantum transport in coupled Majorana box junctions since the corresponding local fermion parities defined above are not conserved anymore. In particular, after a sequence of tunneling events, some of these parities may have been flipped along with a charge transfer between different leads. Similar processes have been discussed in Refs. [61,63] and are known to affect transport properties.

To make progress, it is useful to identify subsets of (MZM and Klein factor) Majorana operators with conserved overall parity. Such a subset must contain an even number m of Majorana operators, where the corresponding Majorana bilinears generate a spin operator with symmetry group SO(m) [53–55,57]. For both cases in Figs. 2(b) and 2(c), three Majorana operators are coupled together at the junction. Taking into account a dummy Majorana mode not shown in Fig. 2, the parity associated with these Majorana states is conserved. As a consequence, the Majorana bilinears resulting from this subset can equivalently be described by Pauli operators $\sigma_{x,y,z}$ as we discuss next.

As a first example, consider the situation in Fig. 2(b), where two Majorana operators (γ_x,γ_y) on the same box (with phase φ conjugate to $\hat{Q}$) are tunnel coupled with amplitudes $\lambda_{x,y}$ to a single lead. The latter is described by the fermion operator $\Psi^\dagger \sim \kappa e^{i\Phi}$. Including for completeness also a finite overlap integral between the MBSs (h_z), the tunneling Hamiltonian (3) for such a junction takes the form

$$\begin{aligned} H_{2,1} &= (\lambda_x\sigma_x + \lambda_y\sigma_y)e^{i(\Phi-\varphi)} + \text{H.c.} + h_z\sigma_z, \\ \sigma_{x,y} &= i\kappa\gamma_{x,y}, \quad \sigma_z = i\gamma_y\gamma_x. \end{aligned} \tag{11}$$

For a specific phase relation between λ_x and λ_y, the same model describes quasiparticle poisoning effects for the single-impurity TKE [63]. As shown in Ref. [63], in the presence of additional leads, the RG flow will generate an additional hybridization term $\sim\sigma_z\Theta'$ between a Pauli operator and the boundary fermion density. In Sec. III D, we will discuss how this finding generalizes to arbitrary complex $\lambda_{x,y}$.

Next we turn to the alternative setup shown in Fig. 2(c), where one MZM (γ) is tunnel coupled to two leads with amplitudes $\lambda_{x,y}$, cf. Ref. [84] for the corresponding $E_C = 0$ case. The respective lead fermions are now written as $\Psi^\dagger_{x,y} \sim \kappa_{x,y}e^{i\Phi_{x,y}}$. From Eq. (3), the tunneling Hamiltonian is then given by

$$H_{1,2} = (\lambda_x\sigma_x e^{i\Phi_x} + \lambda_y\sigma_y e^{i\Phi_y})e^{-i\varphi} + \text{H.c.}, \tag{12}$$

where $\sigma_{x,y} = i\gamma\kappa_{x,y}$. Note that there is no $h_z\sigma_z$ contribution with $\sigma_z = i\kappa_y\kappa_x$. Direct lead-lead tunneling processes (if present) would produce different terms.

We also observe that as long as an arbitrary coupled box system does not admit tunneling paths forming closed loops, all relative phases between tunneling amplitudes can be absorbed by suitable shifts of lead boson fields and thus do not affect the physics. Here closed loop configurations in Hilbert space may arise from ring exchange processes involving several boxes, for instance, a plaquette operator in Majorana code networks [13]. A closed loop is also found for a lead coupled to several MZMs on the same box, see Fig. 2(b). As a consequence, while the relative phase between λ_x and λ_y can be gauged away for the case shown in Fig. 2(c), this is not possible for the setup in Fig. 2(b) anymore.

As a more complicated example for a system with nonsimple contacts, we next consider the two-box setup in Fig. 3. Similar setups arise in basic Majorana qubit and multibox measurements [18,19] and in the context of stabilizer codes [13,14]. Here the left/right ($a = L/R$) box is connected to an

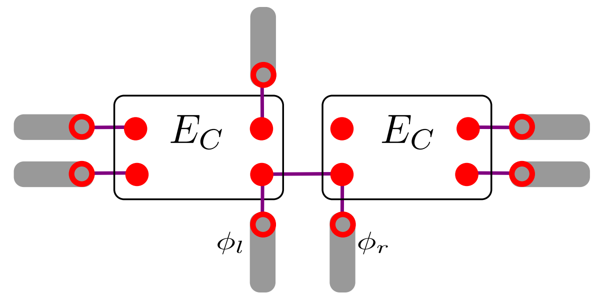

FIG. 3. Two-box setup with a single tunnel bridge connecting the two boxes. Two central leads with boson fields $\Phi_{l,r} = \phi_{l,r}(0)$ are tunnel coupled to the respective MZMs, see Eq. (13). Because of the presence of the MZM-MZM link, those lead-MZM contacts are nonsimple. In addition, $M_{L/R}$ leads are attached to the left/right box via simple contacts, where the shown example is for $M_L = 3$ and $M_R = 2$. For an explanation of symbols, see Figs. 1 and 2.

arbitrary number $M_{L/R}$ of normal leads via simple lead-MZM contacts. Figure 3 shows the case $M_L = 3$ and $M_R = 2$. In addition, two central leads with the respective fermion operator $\Psi^\dagger_{l/r} \sim \kappa_{l/r}e^{i\Phi_{l/r}}$ are connected to the left/right box through nonsimple contacts to the respective MZM operator $\gamma_{l/r}$ (with tunneling amplitude $\lambda_{l/r}$). The contacts are nonsimple because γ_l and γ_r are tunnel coupled by an amplitude t_{LR}. With the box phase operators $\varphi_{L/R}$, the corresponding central part of the coupled device is described by the Hamiltonian

$$\begin{aligned} H_c = {}& t_{LR}\sigma_z e^{i(\varphi_L-\varphi_R)} + \lambda_l\sigma_x e^{i(\varphi_L-\Phi_l)} \\ &+ \lambda_r\sigma_x e^{i(\varphi_R-\Phi_r)} + \text{H.c.}, \end{aligned} \tag{13}$$

where we define $\sigma_z = i\gamma_l\gamma_r$ and $\sigma_x = i\gamma_l\kappa_l$. Note that we can also write $\sigma_x \sim i\gamma_r\kappa_r$ since the central junction parity $\gamma_l\gamma_r\kappa_l\kappa_r = \pm 1$ is conserved. The appearance of different Pauli operators in Eq. (13) suggests that for $\lambda_{l/r} \neq 0$, the two-box setup in Fig. 3 is more difficult to analyze than a purely bosonic counterpart with only simple contacts, e.g., without the central leads in Fig. 3.

D. Quantized box charge and cotunneling operators

Our subsequent discussion will mainly focus on systems where all Majorana boxes are operated at near-integer n_g, i.e., the charge on each box has a quantized ground-state value. As discussed in Sec. II C, while near-degenerate box charge states (with n_g close to half-integer values) can change details of the TKE [64,69], they do not involve additional nonconserved fermion parity degrees of freedom (here represented by Pauli operators). For weak tunneling amplitudes (cf. Sec. II A) and nearly integer n_g on all boxes, the system is described by cotunneling amplitudes connecting in principle any pair of leads in the system via phase-coherent second- or higher-order charge tunneling processes. To obtain the corresponding cotunneling amplitudes in a systematic way, we have employed a Schrieffer-Wolff transformation to project the full theory to the quantized charge ground-state sector of all boxes, see also Refs. [13,14].

The projected cotunneling Hamiltonian will now contain qualitatively different terms. First, there are *purely bosonic* cotunneling contributions. Such processes do not involve Pauli operators representing nonconserved fermion parities and have the schematic form

$$H_{\rm bos} = J_{j_a k_b} e^{i(\Phi_{j_a}-\Phi_{k_b})} + {\rm H.c.},$$
$$J_{j_a k_b} \simeq \frac{\lambda_{j_a j'_a}\lambda^*_{k_b k'_b}}{E_C} \prod_{\langle l,l'\rangle} \frac{t_{ll'}}{E_C}. \tag{14}$$

The cotunneling amplitude $J_{j_a k_b}$ contains the initial and final lead-MZM couplings $\lambda_{j_a j'_a}$ and $\lambda^*_{k_b k'_b}$ for charge tunneling to/from lead j_a/k_b via box a/b, see Eqs. (3) and (8). (Here, $a = b$ is possible.) As a result of the projection to the charge ground-state sector, the $e^{\pm i\varphi_{a/b}}$ terms are not present anymore in Eq. (14) and become effectively replaced by $1/E_C$ factors in the cotunneling amplitude, see Ref. [14]. In order to obtain a contribution for lead pairs attached to different boxes ($a \neq b$), a sequence of intermediate MZM-MZM tunneling events with respective amplitudes $t_{ll'}$, cf. Eq. (2), is necessary. In order to contribute to Eq. (14), however, such MZM-MZM links must have conserved local parities. We also note that since for each additional tunneling event, the contribution to $J_{j_a k_b}$ gets suppressed by a factor $|t_{ll'}|/E_C \ll 1$, the shortest tunneling path(s) between a chosen pair of leads will dominate.

Next, in contrast to the purely bosonic case in Eq. (14), we consider what happens if the tunneling path connecting leads j_a and k_b involves a string of Pauli operators $\sigma^m = \sigma^m_{x,y,z}$. Here σ^m describes the nonconserved local fermion parity at the mth nonsimple link along the path. For a string of $n \geqslant 1$ Pauli operators ($m = 1,\ldots,n$), the projected Hamiltonian has the schematic form

$$H_{\rm nbos} = J^{(\sigma^1,\ldots,\sigma^n)}_{j_a k_b} \sigma^1 \cdots \sigma^n e^{i(\Phi_{j_a}-\Phi_{k_b})} + {\rm H.c.}, \tag{15}$$

where $J^{(\{\sigma\})}_{j_a k_b}$ is a cotunneling amplitude as in Eq. (14) and the superscript serves to remind us that this amplitude applies to a specific tunneling path involving the corresponding Pauli operator string. Concrete examples for this notation will be given in Sec. III and in Appendix A. We note that with the conventions $J^{(\{\sigma\})}_{j_a k_b} \to J_{j_a k_b}$ and $\sigma^1\cdots\sigma^n \to 1$ for $n = 0$, i.e., in the absence of nonsimple links, Eq. (14) constitutes just a special case of Eq. (15).

We close this section by addressing additional complexities in tunneling at a nonsimple junction that comprises multiple Pauli operators of the same set $\sigma_{x,y,z}$. For example, at non-simple contacts in Figs. 2(b) and 2(c), elemental tunneling events may involve anticommuting Pauli operators σ_x and σ_y. The corresponding path contribution now exhibits an extra suppression factor $\sim|\Delta n_g|$, where Δn_g is the detuning of the backgate parameter n_g away from integer values. This suppression arises from the destructive interference between tunneling events with different time ordering [13,14]. In particular, if the box is tuned precisely to a Coulomb valley center, $\Delta n_g = 0$, such paths give no contribution at all. For finite Δn_g, both Pauli operators effectively combine to the third Pauli operator, e.g., $\sigma_x\sigma_y = i\sigma_z$. With this change and including the $|\Delta n_g|$ factor, the cotunneling contribution is then again given by Eq. (15).

Further, in coupled box devices allowing for closed loops, see Sec. II C and Fig. 2(b), elemental tunneling events that connect to distinct MZMs may lead to the same charge transfer. Therefore several distinct paths with different Pauli operator content can contribute to a given cotunneling term $\sim e^{i(\Phi_{j_a}-\Phi_{k_b})}$. Such effects have been exploited, for instance, for Majorana box qubit readout and manipulation schemes [13,14,18,19]. Below we do not consider cases with interfering paths, or if present, as for the loop qubit device in Sec. III D and IV E, we explicitly separate them.

III. RENORMALIZATION GROUP ANALYSIS

Using the composition rules for cotunneling Hamiltonians in Sec. II D, we next turn to the derivation and analysis of the one-loop RG equations. We study general coupled Majorana box devices under Coulomb valley conditions, where nonconserved local fermion parities are described by Pauli operators $\sigma^m = \sigma^m_{x,y,z}$ at the mth link. In Sec. III A, we explain how RG equations for systems of this type can be constructed by using the standard operator product expansion (OPE) technique [70,71]. Subsequently we will study these equations for three device examples in order to illustrate typical effects caused by nonconserved local fermion parities.

A. RG equations: Construction principles

Let us consider the perturbative expansion of the partition function in powers of the cotunneling contributions to the Hamiltonian H, see Eq. (15). The RG approach [71] studies how cotunneling amplitudes are renormalized, and whether new couplings are generated, upon reducing the effective lead bandwidth D from its initial value, $D(\ell = 0) \simeq \min\{E_C,\Delta\}$. Writing $D(\ell) = D(0)e^{-\ell}$, the RG equations describe the physics on lower and lower energy scales with increasing flow parameter ℓ. We show below that always at least a few cotunneling amplitudes will flow towards strong coupling. Since perturbation theory then breaks down at sufficiently low energy scales, the RG approach can only describe the weak-coupling regime. The physics in the strong-coupling regime will be addressed in Secs. IV and V.

In order to obtain RG equations via the OPE approach, one considers arbitrary pairs of cotunneling operators contributing to H. For two operators acting at almost coinciding (imaginary) times τ and τ', the result of such a contraction must be equivalent to a linear combination of all possible operators at time $(\tau+\tau')/2$, where the respective expansion coefficients directly determine the one-loop RG equations [70,71]. We thus have to analyze contractions of cotunneling operator pairs. Denoting the corresponding amplitudes by $J^{(\{\sigma\})}_{jm}$ and $J^{(\{\sigma'\})}_{mk}$, their contraction renormalizes the tunneling amplitude $J^{(\{\sigma''\})}_{jk}$, where the Pauli string $\{\sigma''\}$ follows by multiplication of both operator strings. This composite tunneling amplitude thus connects leads j and k by a tunneling path touching lead m and back. The RG equations now depend on whether the Pauli strings $\sigma^1\cdots\sigma^n$ and $\sigma^{1'}\cdots\sigma^{n'}$ commute or anticommute.

1. Commuting Pauli strings

For commuting Pauli strings, the OPE approach yields the general RG equations (lead density of states $\nu = 1$)

$$\frac{dJ^{(\{\sigma''\})}_{jk}}{d\ell} = \sum_{m\neq(j,k)} J^{(\{\sigma\})}_{jm} J^{(\sigma')}_{mk}. \tag{16}$$

This result is simple to understand if both Pauli strings do not share overlapping Pauli operators at all. The composite tunneling path is then obtained by simply stitching together both paths, and the Pauli string $\{\sigma''\}$ corresponds to the product of the strings $\{\sigma\}$ and $\{\sigma'\}$. Moreover, if identical Pauli operators appear in both strings, say, σ_x^m and $\sigma_x^{m'=m}$, they effectively square to unity and thus drop out in the string $\{\sigma''\}$. Let us now discuss Eq. (16) in more detail for different cases of interest.

To that end, it is very convenient to introduce the concept of *bosonic subsectors* (or simply subsectors). A bosonic subsector $\mathcal{B}$ refers to a group of M leads (with index $j \in \mathcal{B}$) which are coupled to each other through purely bosonic cotunneling processes, and hence undergo purely bosonic interactions within the subsector, cf. Eq. (14). For example, this happens for simply-coupled leads that are attached to the same box. If two leads cannot be connected via purely bosonic cotunneling processes, i.e., if a Pauli string is involved, they must belong to distinct subsectors. In particular, a lead with a nonsimple lead-MZM contact generally defines its own subsector with $M = |\mathcal{B}| = 1$. According to this definition, all leads in a general Majorana network uniquely belong to one of its corresponding subsectors.

We start with the case of M leads attached to a given box via simple lead-MZM contacts, thus forming a subsector $\mathcal{B}$. In the simplest case, the Hamiltonian describing purely bosonic cotunneling processes within this subsector follows from Eq. (14) by summing over all tunneling paths connecting lead $j \neq k$ (with $j,k \in \mathcal{B}$). Such processes have amplitude J_{jk} and couple different leads only via the lead boson fields Φ_j and Φ_k. Adapting Eq. (16) to this purely bosonic problem, we reproduce the RG equations for the single-impurity TKE [53–57],

$$\frac{dJ_{jk}}{d\ell} = \sum_{m\in\mathcal{B},m\neq(j,k)} J_{jm}J_{mk}. \tag{17}$$

For $M \geqslant 3$, these couplings automatically scale towards isotropy, $J_{jk}(\ell) \to (1-\delta_{jk})J(\ell)$, see Refs. [53,56] for a detailed discussion. The RG equation for the isotropic coupling J is then given by $dJ/d\ell = (M-2)J^2$. The isotropic part is thus marginally relevant and flows towards strong coupling. Deviations from isotropy, on the other hand, are RG irrelevant and can be neglected at low energy scales. The TKE thus features an in-built flow to isotropy. The strong-coupling regime is reached at energy scales below the Kondo temperature [53–55]

$$T_K \simeq De^{-1/[(M-2)\nu J]}, \tag{18}$$

where D is the (bare) bandwidth of the leads, and for completeness we reinserted the lead density of states ν.

Apart from the purely bosonic processes behind Eq. (17), cotunneling events also can kick the system out of a bosonic subsector $\mathcal{B}_1$ into a distinct subsector $\mathcal{B}_2$, which may belong to the same or to another box. By definition, such processes involve a string $\sigma^1\cdots\sigma^n$ of $n \geqslant 1$ Pauli operators. The corresponding Hamiltonian reads, cf. Eq. (15),

$$H_{\rm nbos} = \sum_{j\in\mathcal{B}_1}\sum_{k\in\mathcal{B}_2} J_{jk}^{(\{\sigma\})}\sigma^1\cdots\sigma^n e^{i(\Phi_j-\Phi_k)} + \text{H.c.} \tag{19}$$

In Appendix A, we illustrate several examples for tunneling processes contributing to Eq. (19) in a rather advanced device with four boxes. These examples also serve to show the general applicability and versatility of our formalism for arbitrary coupled box devices.

We now study how the RG equations in Eq. (17) for purely bosonic couplings J_{jk} with $j \neq k \in \mathcal{B}$ will be modified by the intersubsector cotunneling processes in Eq. (19). In general, such an excursion from lead $j \in \mathcal{B}$ to some other subsector $\mathcal{B}_2$ must involve a Pauli string $\sigma^1\cdots\sigma^n$ with $n \geqslant 1$. In order to contribute to the RG flow of our purely bosonic coupling J_{jk}, however, the tunneling path must now return to lead $k \in \mathcal{B}$ via the *same* Pauli operator string. As a result, for coupled-box networks, the RG equations for the TKE in Eq. (17) receive an additional contribution,

$$\frac{dJ_{jk}}{d\ell} = \sum_{m\in\mathcal{B},m\neq(j,k)} J_{jm}J_{mk} + \sum_{m\notin\mathcal{B}} J_{jm}^{(\{\sigma\})}J_{mk}^{(\{\sigma\})}. \tag{20}$$

Similarly, see also Appendix A for additional details, we obtain the RG equations for the cotunneling amplitudes $J_{jk}^{(\{\sigma\})}$, with leads $j \in \mathcal{B}_1$ and $k \in \mathcal{B}_2$ belonging to different subsectors, from the general equations (16),

$$\frac{dJ_{jk}^{(\{\sigma\})}}{d\ell} = \sum_{m\in\mathcal{B}_2,m\neq k} J_{jm}^{(\{\sigma\})}J_{mk} + \sum_{m\in\mathcal{B}_1,m\neq j} J_{jm}J_{mk}^{(\{\sigma\})}. \tag{21}$$

The first (second) term comprises an intersector transition followed by an intrasector tunneling in $\mathcal{B}_2$ ($\mathcal{B}_1$). We note that on top of the terms in Eq. (21), higher-order tunneling excursions via distinct subsectors $\mathcal{B}' \neq \mathcal{B}_{1,2}$ may generate additional contributions, see Appendix A. For the applications below, such complications are absent.

2. Anticommuting Pauli strings

Next we discuss the case of anticommuting Pauli strings $\{\sigma\}$ and $\{\sigma'\}$. Using the relation $\mathcal{T}_\tau\sigma_x(\tau)\sigma_y(\tau') = i\sigma_z(\tau)\text{sgn}(\tau-\tau')$ for $\tau\to\tau'$ (and cyclic permutations thereof), with the time-ordering operator $\mathcal{T}_\tau$, we first observe that contributions with different time ordering will interfere destructively. As a consequence, we find that there will be no additional contributions to the RG equations (20) and (21) from such tunneling events.

However, other types of RG terms can be generated in systems allowing for closed loops, where subsectors can be connected through distinct tunneling paths with different Pauli strings. To that end, let us pick a tunneling path which starts at lead $j \in \mathcal{B}$, makes an excursion to a lead in some other subsector, $l \notin \mathcal{B}$, and phase-coherently returns back to lead j. To illustrate the principle, we here focus on the simplest scenario, where the Pauli strings $\{\sigma'\}$ and $\{\sigma\}$ for back-and-forth tunneling, respectively, are identical except at one link (m). At this link, we have anticommuting Pauli operators, say, σ_x^m and σ_y^m. Contracting both cotunneling operators now schematically yields

$$\begin{aligned} &J_{jl}^{(\ldots\sigma_x^m\ldots)}(\cdots\sigma_x^m\cdots)_\tau J_{lj}^{(\ldots\sigma_y^m\ldots)}(\cdots\sigma_y^m\cdots)_{\tau'} \\ &\quad\sim J_{jl}^{(\ldots\sigma_x^m\ldots)}J_{lj}^{(\ldots\sigma_y^m\ldots)}\, i\sigma_z^m(\tau)\text{sgn}(\tau-\tau'), \end{aligned} \tag{22}$$

where all other Pauli operators apart from $\sigma^m_{x,y}$ square out. Expanding also the $e^{\pm i\Phi_j}$ factors appearing in all cotunneling operators to lowest order in $\tau-\tau'$, we encounter another $\mathrm{sgn}(\tau-\tau')$ factor and therefore a finite contribution to the RG equations. Using the lead densities near the respective contacts, $\Theta'_j(\tau)=\partial_x\theta_j(x=0,\tau)=-i\partial_\tau\phi_j(x=0,\tau)$, see Eq. (6), we then obtain a new contribution generated by such contractions,

$$H_{\rm hyb}=\sum_j \Lambda_j\sigma^m_z\Theta'_j, \tag{23}$$

describing a hybridization between σ^m_z and the lead fermion densities Θ'_j. (Of course, depending on the application, the coupling in Eq. (23) may involve other or even multiple Pauli operators.) We note that similar terms also appear in the context of charge Kondo effects [70,79,83].

From Eq. (22), the RG flow of the coupling constants in Eq. (23) is then governed by

$$\frac{d\Lambda_j}{d\ell}\sim\sum_{l\notin\mathcal{B}} J^{(\ldots\sigma^m_x\ldots)}_{jl}J^{(\ldots\sigma^m_y\ldots)}_{lj}+\text{H.c.} \tag{24}$$

Hybridization couplings thus will be dynamically created during the RG flow even for vanishing bare coupling, i.e., for $\Lambda_j(\ell=0)=0$. We remark in passing that $\Lambda_j(0)\neq 0$ could arise from in- and out-tunneling events at a lead contacting several MZMs, cf. Fig. 2(b). The Λ_j are real-valued couplings which are effectively controlled by the sine or cosine of the loop phase

$$\varphi^{\rm loop}_j=\arg\left(\sum_{l\notin\mathcal{B}} J^{(\ldots\sigma^m_x\ldots)}_{jl}J^{(\ldots\sigma^m_y\ldots)}_{lj}\right). \tag{25}$$

Importantly, the hybridizations in turn feed back into the RG equations (21) for cotunneling amplitudes. In fact, we find that Eq. (21) receives the additional contributions

$$\frac{dJ^{(\ldots\sigma^m_{x/y}\ldots)}_{jl}}{d\ell}\sim(\Lambda_l-\Lambda_j)J^{(\ldots\sigma^m_{y/x}\ldots)}_{jl}. \tag{26}$$

For the loop qubit example studied below, see Secs. III D and IV E, such RG feedback effects turn out to be crucial.

3. Summary

The above rules show that RG equations for a general coupled Majorana box system can be determined by contracting pairs of tunneling operators. Commuting tunneling operators generate new composite tunneling operators and/or renormalize existing couplings, see Eqs. (20) and (21). Contractions of noncommuting operators, on the other hand, do not contribute to the latter RG equations. However, in systems with tunneling paths forming closed loops, hybridization terms between Pauli operators and lead fermion densities will be generated. Such terms will in turn feed back into the RG equations for the cotunneling amplitudes. Next we apply the above RG analysis to several examples of practical interest.

B. Two-box device

Let us begin by studying a two-box device as shown in Fig. 3. We first observe that such a system does not admit tunneling paths forming closed loops, and thus the RG equations do not involve the hybridizations in Eq. (23). Using $H_{\rm leads}$ in Eq. (7) and taking into account the central junction described by Eq. (13), the Hamiltonian $H=H_{\rm leads}+H_L+H_R+H_{LR}$ is obtained by a Schrieffer-Wolff transformation to the ground-state charge sector of both boxes, see Sec. II D. In particular, cotunneling processes involving only boson fields connected to the left/right (L/R) box are contained in

$$\begin{aligned}H_{L/R}=&-\sum_{j,k\in\mathcal{B}_{L/R},j\neq k}(J_{L/R})_{jk}\cos(\Phi_j-\Phi_k)\\&-\sum_{j\in\mathcal{B}_{L/R}}(J_X)_{l/r,j}\sigma_x\cos(\Phi_{l/r}-\Phi_j),\end{aligned} \tag{27}$$

where $\mathcal{B}_{L/R}$ denotes bosonic subsectors with $M_{L/R}$ leads connected to the respective box via simple lead-MZM contacts. (For the example in Fig. 3, $M_L=3$ and $M_R=2$.) The central leads in Fig. 3, with boson fields $\Phi_{l/r}$, are coupled to the L/R box via nonsimple contacts, where nonconserved local fermion parities are encoded by the Pauli operators $\sigma_{x,y,z}$, see Eq. (13). Interbox cotunneling processes are contained in

$$\begin{aligned}H_{LR}=&-\sum_{j\in\mathcal{B}_L}(J_Y)_{rj}\,\sigma_y\cos(\Phi_r-\Phi_j)\\&-\sum_{k\in\mathcal{B}_R}(J_Y)_{lk}\,\sigma_y\cos(\Phi_l-\Phi_k)\\&+\sum_{j\in\mathcal{B}_L,k\in\mathcal{B}_R}(J_Z)_{jk}\,\sigma_z\sin(\Phi_j-\Phi_k).\end{aligned} \tag{28}$$

The $J_{L/R}$ amplitudes in Eq. (27) are purely bosonic intrasector couplings as in Sec. III A. The J_X (resp., J_Y) cotunneling amplitudes connect leads within bosonic subsector $\mathcal{B}_{L/R}$ to the central lead on the same (resp., other) box, involving the Pauli string σ_x (resp., σ_y). Finally, the J_Z amplitudes link the bosonic subsectors $\mathcal{B}_L$ and $\mathcal{B}_R$ by interbox tunneling via the Pauli string σ_z.

In total, we thus have seven coupling families: $J_{L/R},J_{X,l/r},J_{Y,r/l}$, and J_Z. The respective coupling matrix elements depend on microscopic lead-MZM (λ_j) and MZM-MZM (t_{LR}) tunneling amplitudes, cf. Eq. (13). Schematically, $(J_{L/R/X})_{jk}\sim\lambda_j\lambda^*_k/E_C$ and $(J_{Y/Z})_{jk}\sim\lambda_j\lambda^*_k t_{LR}/E^2_C$. Since one can gauge away complex phases of tunneling amplitudes for systems without closed loops, all these cotunneling amplitudes can be chosen real positive. Within each coupling family, we thus arrive at a real symmetric matrix.

The RG equations then follow from Eqs. (20) and (21). For $j,k\in\mathcal{B}_L$, we find

$$\begin{aligned}\frac{d(J_L)_{jk}}{d\ell}=&\sum_{m\in\mathcal{B}_L,m\neq(j,k)}(J_L)_{jm}(J_L)_{mk}+(J_X)_{lj}(J_X)_{lk}\\&+(J_Y)_{rj}(J_Y)_{rk}+\sum_{m\in\mathcal{B}_R}(J_Z)_{jm}(J_Z)_{mk}.\end{aligned} \tag{29}$$

Furthermore, with $j\in\mathcal{B}_L$, we get

$$\frac{d(J_{X/Y})_{l/r,j}}{d\ell}=\sum_{m\in\mathcal{B}_L,m\neq j}(J_{X/Y})_{l/r,m}(J_L)_{mj}, \tag{30}$$

while for $j \in \mathcal{B}_L$ and $k \in \mathcal{B}_R$,

$$\frac{d(J_Z)_{jk}}{d\ell} = \sum_{m\in\mathcal{B}_L,m\neq j} (J_L)_{jm}(J_Z)_{mk} + \sum_{m\in\mathcal{B}_R,m\neq k} (J_Z)_{jm}(J_R)_{mk}. \quad (31)$$

The corresponding RG equations for the J_R, $J_{X,r}$, and $J_{Y,l}$ couplings follow by exchanging left/right labels.

The above RG equations can be simplified considerably by observing that different coupling families effectively become isotropic at low energy scales. For small-to-moderate bare anisotropies of the respective coupling matrices, such an isotropization can already be established within the weak-coupling regime accessible to the RG approach. For the single-box TKE case with $M \geqslant 3$ leads, this mechanism has been detailed in Refs. [53–56]. As shown in Appendix B by a numerical solution of the full RG equations (29)–(31), the isotropization mechanism also applies for the two-box device in Fig. 3 with $M_R = 2$. By a similar analysis, we have verified that isotropization applies for all other examples where we invoke it below. This finding can be rationalized by noting that for any $M \geqslant 2$, couplings to leads in this sector feed back into the RG flow of each other if they belong to the same family. As a consequence, different coupling families are effectively described by specifying only their mean (average) values, $(J_L)_{jk} \to J_L$ and so on, see Eq. (B1) in Appendix B. Anisotropies within a given coupling family are RG irrelevant and thus can be neglected at low energies. In fact, we expect the above conclusions to apply for general coupled Majorana box systems.

The two-box problem in Fig. 3 is then described by seven running couplings, where Eqs. (29)–(31) yield the isotropized RG equations

$$\frac{dJ_L}{d\ell} = (M_L-2)J_L^2 + M_R J_Z^2 + J_{X,l}^2 + J_{Y,r}^2,$$
$$\frac{dJ_{X,l}}{d\ell} = (M_L-1)J_{X,l}J_L, \quad \frac{dJ_{Y,r}}{d\ell} = (M_R-1)J_{Y,r}J_L,$$
$$\frac{dJ_Z}{d\ell} = [(M_L-1)J_L + (M_R-1)J_R]J_Z, \quad (32)$$

and related equations for J_R, $J_{X,r}$, and $J_{Y,l}$. Let us briefly check Eq. (32) for two limiting cases:

(i) For vanishing MZM-MZM coupling, $t_{LR} \to 0$, both boxes are decoupled. We thus have $J_Z = J_{Y,r/l} = 0$, and $\sigma_x = \pm 1$ is conserved. The above equations then reduce to a decoupled pair of single-impurity TKE systems, cf. Eq. (17), where $M_L + 1$ and $M_R + 1$ leads are attached to the left/right box: For $t_{LR} = 0$, the central leads l and r in Fig. 3 join the respective bosonic subsector $\mathcal{B}_{L/R}$.

(ii) In the absence of both central leads, we have $J_{X,l/r} = J_{Y,r/l} = 0$ and $\sigma_z = \pm$ is conserved. In that case, we recover the RG equations for the single-impurity TKE again. However, since both boxes are now connected by $t_{LR} \neq 0$, we encounter the equations for a *single* Kondo impurity with $M_L + M_R$ attached leads. At low energies, both boxes are thus fused together by the MZM-MZM link and thereby form a single enlarged Majorana box that subsequently exhibits a global TKE with symmetry group $SO_2(M_L + M_R)$.

For generic initial values of the isotropized cotunneling amplitudes, we have numerically solved the RG equations (32). Our analysis shows that the system will flow towards strong coupling with competing separate (intrabox) and global (interbox) TKEs. This scenario is reminiscent of the classic two-impurity Kondo problem [76–78] and indicates that a strong-coupling analysis is needed in order to determine the ground state, see Sec. IV C.

C. MZM coupled to multiple leads

An interesting limit of the two-box RG equations (32) concerns the physics of a single MZM coupled to several leads, see Fig. 2(c) and Eq. (12). To this end, one may consider a situation where the left (resp., right) box has $M \equiv M_L$ (resp., $M_R = 1$) leads with simple lead-MZM contacts. These leads are described by the boson fields $\Phi_{j\in\mathcal{B}_L}$ (resp., Φ_z). We then note that the MZM γ_l on the left box, which is tunnel coupled to the central lead $\Phi_x \equiv \Phi_l$ in Fig. 3, effectively also couples to the two leads connected to the right box via the MZM-MZM tunnel bridge. Let us write $\Phi_y \equiv \Phi_r$ for the corresponding central lead and use isotropic couplings for different coupling families, see Sec. III B, where isotropization holds for $M \geqslant 2$. Retaining for the moment only the four couplings

$$J = J_L, \quad J_x = J_{X,l}, \quad J_y = J_{Y,r}, \quad J_z = J_Z, \quad (33)$$

the low-energy Hamiltonian is $H = H_{\rm leads} + H_b$, with the boundary term

$$H_b = -J \sum_{j,k\in\mathcal{B}_L,j\neq k} \cos(\Phi_j - \Phi_k) - \sum_{\alpha=x,y,z} J_\alpha \sigma_\alpha \sum_{j\in\mathcal{B}_L} \cos(\Phi_j - \Phi_\alpha). \quad (34)$$

The J_α in Eq. (33) thus characterize our lead-MZM multijunction. We emphasize that the right box in the above setup is not necessary for observing the physics below, and one could simply couple the leads corresponding to the fields $\Phi_{x,y,z}$ directly to γ_l. Its inclusion here only allows us to take over results from Sec. III B.

In fact, the corresponding RG equations can now be read off from Eq. (32),

$$\frac{dJ}{d\ell} = (M-2)J^2 + \sum_\alpha J_\alpha^2, \quad \frac{dJ_\alpha}{d\ell} = (M-1)JJ_\alpha. \quad (35)$$

Cotunneling processes between the three leads $\Phi_{x,y,z}$ are not contained in Eq. (34) and arise due to the three remaining couplings J_R, $J_{X,r}$, and $J_{Y,l}$ beyond those in Eq. (33). Such terms generate the additional contribution $H_b' \sim \sigma_z \cos(\Phi_x - \Phi_y)$ plus cyclic permutations. From the analysis in Sec. II D, we find $H_b' = 0$ under Coulomb valley center conditions, i.e., for $\Delta n_g = 0$. In any case, such couplings are neither RG relevant, in contrast to those in Eq. (33), nor do they enter the flow of other couplings in Eq. (35). We can thus safely drop them in what follows.

Let us then discuss the RG flow generated by Eq. (35). First, we observe that ratios of different J_α couplings are conserved, $dJ_x/dJ_y = J_x(0)/J_y(0)$ and $dJ_y/dJ_z = J_y(0)/J_z(0)$. All J_α therefore flow towards strong coupling together with those ratios being invariant. Second, for $M \geqslant 3$, the TKE-like coupling

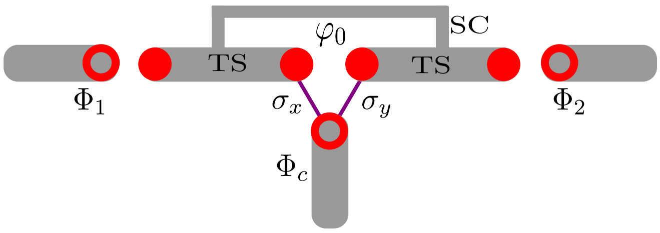

FIG. 4. Loop qubit device contacted by normal leads. This device has been suggested in Fig. 14 of Ref. [19] for interferometric Majorana qubit measurements and manipulations, see also Refs. [13,14,18]. Two long topological superconductor (TS) wires with a superconducting (SC) bridge define a Majorana box with four MZMs, where the loop phase φ_0 can be controlled by a magnetic flux. The normal leads attached to the box correspond to boson fields $\Phi_{1,2,c}$. The central lead (Φ_c) couples to two MZMs as in Fig. 2(b), where the nonconserved fermion parity is encoded by Pauli operators $\sigma_{x,y,z}$. For an explanation of symbols, see Figs. 1 and 2.

J outgrows the J_α since they all feed back into the RG flow of J. In contrast, for $M = 2$, we observe that J does not benefit from the self-enhanced TKE-like RG flow, cf. Eq. (17), and therefore will not automatically dominate anymore. In fact, for $M = 2$, Eq. (35) becomes a multicomponent version of the celebrated Kosterlitz-Thouless equations [71], where the RG flow of J is directly induced by the J_α flow and vice versa. In our strong-coupling analysis of this setup, see Sec. IV D, we will focus on the most interesting case $M = 2$. Further transport properties for this system are discussed in Sec. V.

D. Loop qubit

As a final example for the RG analysis, we here consider the loop qubit device shown in Fig. 4. This device has a single Majorana box containing $M = 2$ leads with simple contacts, and a nonsimple contact coupling two MZMs to a central lead (with boson field Φ_c), see Sec. II C, in particular Eq. (11) and Fig. 2(b). Importantly, such a device provides the simplest possibility for tunneling paths forming closed loops. It has been suggested as Majorana qubit realization [19], where the relative phase φ_0 between the tunneling amplitudes connecting the central lead with the respective MZM can be changed by a magnetic flux. We note that φ_0 corresponds to the loop phase between different tunneling paths in Eq. (25). By contacting the box with leads as shown in Fig. 4, nontrivial interferometric conductance measurements can be performed. In particular, a measurement of the linear conductance between the central lead and one of the outer leads ($\Phi_{1,2}$ in Fig. 4) could determine the eigenvalue of the Pauli operator σ_z related to the nonconserved fermion parity of the junction [18,19].

The nonsimple junction is described by $H_{2,1}$ in Eq. (11) with $\Phi \to \Phi_c$ and $h_z \to 0$. We do not include a direct MZM-MZM coupling, but MZMs instead hybridize with the fermion density at the central contact, see below. With $\sigma_\pm = (\sigma_x \pm i\sigma_y)/2$, we thus have

$$H_{2,1} = (\lambda_+\sigma_+ + \lambda_-\sigma_-)e^{i(\varphi-\Phi_c)} + \text{H.c.},$$
$$\lambda_\pm = \lambda_x \mp i\lambda_y e^{i\varphi_0}, \tag{36}$$

where we use a gauge where φ_0 appears at the σ_y link in Fig. 4 and the tunneling amplitudes $\lambda_{x,y}$ are real valued. Interestingly, for $\varphi_0 = \pi/2$, the same model describes quasiparticle poisoning effects for the TKE [63].

As the next step, we implement the projection to the ground-state charge of the box, see Sec. II D. Following the corresponding steps in Ref. [63] but allowing for arbitrary loop phase φ_0, we then get the Hamiltonian $H = H_{\text{leads}} + H_b$. For M leads (labeled by $j \in \mathcal{B}$) with simple contacts to the box, where $M = 2$ in Fig. 4,

$$H_b = -J \sum_{j,k\in\mathcal{B}, j\neq k} \cos(\Phi_j - \Phi_k) - \sum_{j\in\mathcal{B}} \tilde{\Lambda}\sigma_z\Theta'_j - \Lambda_c\sigma_z\Theta'_c$$
$$- \frac{1}{\sqrt{2}} \sum_{j\in\mathcal{B}} [(L_+\sigma_+ + L_-\sigma_-)e^{i(\Phi_j-\Phi_c)} + \text{H.c.}], \tag{37}$$

where we assume isotropic couplings. With a tunnel coupling $\tilde{\lambda}$ for the simple lead-MZM contacts, the complex-valued cotunneling amplitudes between the central and the outer leads are contained in $L_\pm = \sqrt{2}\tilde{\lambda}\lambda_\pm/E_C$, see Eq. (36). In contrast, the TKE-like coupling J describes cotunneling between leads within subsector $\mathcal{B}$. Because of the existence of tunneling paths forming closed loops, Eq. (37) also contains hybridization terms of the form in Eq. (23). The bare (initial) values for these couplings are $\tilde{\Lambda} = 0$ and $\Lambda_c \simeq (\lambda_x\lambda_y/E_C)\sin\varphi_0$. During the RG flow, both $\tilde{\Lambda}$ and Λ_c grow and approach strong coupling.

We next exploit current conservation, $\langle\Theta'_c\rangle + \sum_j \langle\Theta'_j\rangle = 0$, which follows from gauge invariance under a simultaneous shift of all boson fields $\Phi_{j,c}$. This relation allows us to further reduce the number of parameters by trading off hybridizations at the outer leads versus an enhanced hybridization between the central lead and σ_z. With $\Lambda = 2(\Lambda_c - \tilde{\Lambda})$, we then obtain the RG equations, cf. Ref. [63],

$$\frac{dJ}{d\ell} = (M-2)J^2 + |L_+|^2 + |L_-|^2,$$
$$\frac{dL_\pm}{d\ell} = [(M-1)J \pm \Lambda]L_\pm,$$
$$\frac{d\Lambda}{d\ell} = (M+1)(|L_+|^2 - |L_-|^2). \tag{38}$$

The most interesting prediction of these equations is the onset of *helicity* [63], i.e., a nontrivial flow of the couplings $L_\pm$. To this end, it is instructive to relate the RG flow of the above couplings with that of the loop phase φ_0. We first observe that with $\lambda_\pm$ in Eq. (36),

$$|L_+(\ell)|^2 + |L_-(\ell)|^2 \sim \lambda_x^2 + \lambda_y^2,$$
$$|L_+(\ell)|^2 - |L_-(\ell)|^2 \sim \lambda_x\lambda_y \sin\varphi_0. \tag{39}$$

This implies that while the TKE-like coupling J grows and stays independent of φ_0, the hybridization Λ, with initial value $\Lambda(\ell = 0) \sim \sin\varphi_0$, keeps the same dependence on φ_0 throughout the RG flow. Moreover, the complex phases of the couplings $L_\pm$ are invariant during the RG flow since the prefactor for their self-renormalization in Eq. (38) is real. Using $L_\pm \sim \lambda_\pm$, the running loop phase is then defined by

$$\varphi_0(\ell) = \arg[i(L_+ - L_-)/(L_+ + L_-)]_\ell. \tag{40}$$

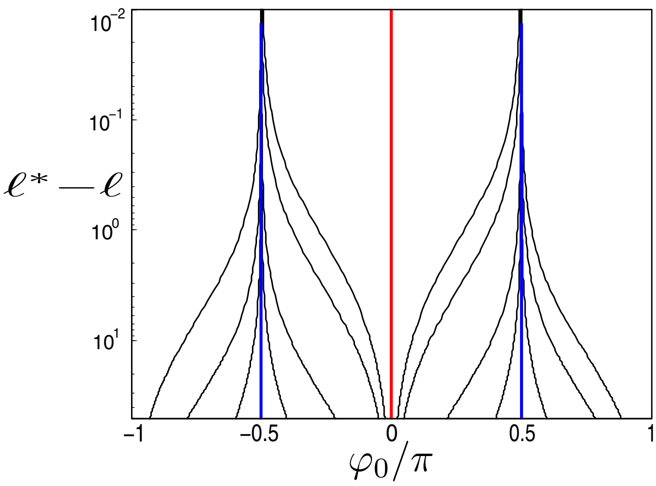

FIG. 5. RG flow of the loop phase $\varphi_0(\ell)$ obtained by numerical integration of a fully anisotropic version [63] of the RG equations (38). At $\ell = \ell^*$, the RG approach breaks down due to divergent couplings. We show results for $\ell^* - \ell$ vs φ_0 on a semilogarithmic scale. While this plot was generated for a specific randomly chosen set of initial parameters, with different $\varphi_0(0)$, we have checked that the qualitative features of the RG flow are insensitive to this choice. We identify two stable fixed points with $\varphi_0 = \varphi_\pm = \pm\pi/2$ (blue vertical lines), where the hybridization is maximized, $\Lambda(\ell) \sim \sin\varphi_0(\ell)$. In contrast, $\varphi_0 = 0 \bmod \pi$ (red vertical line) are unstable fixed points with $\Lambda = 0$. The gauge symmetry of the system under the exchange $L_+ \leftrightarrow L_-$, $\sigma_+ \leftrightarrow \sigma_-$, and $\sigma_z \to -\sigma_z$, cf. Eqs. (37) and (38), is apparent in the symmetry of the RG flow under $\varphi_0 \to -\varphi_0$.

Note that $\varphi_0(\ell)$ will in general change during the RG flow because it depends on both the complex phases and the absolute values of $L_\pm$. In particular, we observe that for bare loop phases with $\varphi_0(0) \in (0,\pi)$, we will also have $|L_+(0)| > |L_-(0)|$, while for $\varphi_0(0) \in (-\pi,0)$, we instead find $|L_-(0)| > |L_+(0)|$. The RG equations (38) thus predict a flow of the bigger coupling $L_\pm$ to strong coupling, along with growing J and Λ, while the opposite coupling $L_\mp$ is dynamically suppressed.

In Fig. 5, we show typical results for the RG flow of φ_0 obtained by numerical integration of a fully anisotropic version of Eq. (38). The numerical results perfectly recover the qualitative behavior discussed above. We note that these calculations have also confirmed that all couplings indeed become isotropic during the RG flow. In physical terms, the limiting cases of the RG flow in Fig. 5 correspond to phase pinning at low energies, with the stable asymptotic value $\varphi_\pm = \pm\pi/2$ as $L_\pm$ outgrows $L_\mp$, cf. Eq. (40). These two values correspond to the helical fixed points found in Ref. [63].

Instead, for $\varphi_0 = 0$ or $\varphi_0 = \pi$, the RG flow of the hybridization, $\Lambda(\ell) \sim \sin\varphi_0(\ell) = 0$, is fully blocked. Remarkably, in terms of $J_x = (L_+ + L_-)/2$ and $J_y = -i(L_+ - L_-)/2$, we now recover the RG equations (35) for the fundamentally different problem of a single MZM coupled to two leads. These flow equations (with $J_z = 0$) imply a flow to strong coupling of J and $J_{x,y}$, with fixed ratio J_x/J_y, see Sec. III C. We will return to the loop qubit device in our discussion of the strong-coupling limit in Sec. IV E.

IV. STRONG-COUPLING REGIME

In Sec. III we have seen that, in general, the systems studied here will approach the strong-coupling regime. At very low energies, in particular for an understanding of the ground state, one therefore has to go beyond the RG approach. In this section, we extend concepts developed for a strong-coupling solution of the TKE via Abelian bosonization [54–58,67] to our more general setting. Such strategies can lead to additional insights and even allow for analytical solutions in not too complicated setups.

The arguments in Sec. III imply that at low energy scales, we need to keep only isotropic cotunneling amplitudes within and in between subsectors. In fact, if a subsector contains more than one lead, the center-of-mass field will be the only linear combination that is not pinned in the ground state. To access the ground state, we thus need to study the combined dynamics of these center-of-mass fields and the Pauli operator strings in the system. In this way, the complexity of the problem can be drastically reduced and the physics becomes more transparent, see Sec. IV A. A second key ingredient of our strong-coupling approach is tied to the possibility of decoupling certain linear combinations of boson fields via unitary transformations, see Sec. IV B. We illustrate this strategy in Secs. IV C–IV E for the three applications discussed from the RG viewpoint in Secs. III B–III D.

A. Reduction of bosonic subsectors

Our first step in the construction of the strong-coupling theory is the reduction of every bosonic subsector $\mathcal{B}$ to the corresponding center-of-mass field,

$$\phi_0(x,\tau) = g_0 \sum_{j\in\mathcal{B}} \phi_j(x,\tau), \quad g_0 = \frac{1}{\sqrt{M}}, \tag{41}$$

where $\Phi_0 = \phi_0(x=0)$. For $M = 1$, the field Φ_0 then just coincides with the single boson field in the respective subsector (with $g_0 = 1$), but Eq. (41) implies a reduction of complexity for $M = |\mathcal{B}| \geqslant 2$. The usefulness of Eq. (41) follows from previous Abelian bosonization studies of the strong-coupling TKE [54,55,64,67,69] and from our arguments in Sec. III. In fact, for $M \geqslant 2$, couplings within $\mathcal{B}$ grow strong, and for $M \geqslant 3$ also become isotropic. (However, isotropy is not necessary for our discussion below.) In detail, following Refs. [54–56], we introduce reduced boson fields, $\tilde{\Phi}_{j\in\mathcal{B}} = \Phi_j - g_0\Phi_0$, with the constraint $\sum_j \tilde{\Phi}_j = 0$. Next, we recall that intrasubsector cotunneling amplitudes J_{jk} (with $j,k \in \mathcal{B}$) can be chosen real positive upon absorbing tunnel phases into lead phase fields. We hence obtain the Hamiltonian for the subsector as

$$H_{\mathcal{B}} = -\sum_{j,k\in\mathcal{B},j\neq k} J_{jk}\cos(\tilde{\Phi}_j - \tilde{\Phi}_k). \tag{42}$$

At strong coupling, the low-energy physics in $\mathcal{B}$ exhibits an analogy to the quantum Brownian motion of a particle with coordinates $\tilde{\Phi}_j$ in the $(M-1)$-dimensional lattice defined by the potential $H_{\mathcal{B}}$ [54–56,74,75]. The motion along the Φ_0 direction is analogous to that of a free particle with linear dispersion, inherited from the free boson theory in Sec. II B. In particular, Eq. (42) does not introduce an energy cost along this direction. The free field Φ_0 thus dominates the low-energy physics. The leading irrelevant operators at the strong-coupling fixed point then come from tunneling events connecting neighboring lattice minima [74,75], corresponding to quantum phase slips between static configurations $\{\tilde{\Phi}_j\} \equiv \{\tilde{\varphi}_j\}$ minimizing $H_{\mathcal{B}}$ under the constraint $\sum_j \tilde{\varphi}_j = 0$. Such phase slips can be triggered by electron-hole pair excitations (causing Ohmic dissipation) in the leads [54,55], or due to an applied bias voltage [67]. In fact, scaling dimensions of non-Fermi liquid corrections at the strong-coupling point can be obtained by a geometric analysis of the lattice potential in Eq. (42) [74,75].

Our main interest in this paper is not in effects caused by such intrasubsector leading irrelevant operators. Instead, we want to clarify how different center-of-mass boson fields in a coupled box device interact among themselves and with Pauli string operators. We thus assume that all reduced fields in bosonic subsectors are pinned to their static quasiclassical minima, and then express the dynamics of Φ_j in terms of the center-of-mass motion,

$$\Phi_{j\in\mathcal{B}}(\tau) = \tilde{\varphi}_j + g_0\Phi_0(\tau). \tag{43}$$

We note that Eq. (43) is appropriate for ground-state properties but misses the leading irrelevant operators discussed above. However, their effects are quite well understood and in any case could be added *a posteriori* via perturbation theory. Let us now consider the effects of the projection in Eq. (43) on intersubsector coupling terms. Inserting Eq. (43) into Eq. (19), for transitions between subsectors $\mathcal{B}_1$ and $\mathcal{B}_2$, we find the term

$$H_{\mathcal{B}_1,\mathcal{B}_2} = \sum_{j\in\mathcal{B}_1}\sum_{k\in\mathcal{B}_2} J_{jk}^{(\{\sigma\})}\sigma^1\cdots\sigma^n e^{i(\tilde{\varphi}_j-\tilde{\varphi}_k)}e^{i(g_1\Phi_1-g_2\Phi_2)}, \tag{44}$$

where $\Phi_{1,2}$ denote the center-of-mass fields for subsectors $\mathcal{B}_{1,2}$, respectively, with $g_{1,2}$ in Eq. (41).

Since in Eq. (42) we gauged away relative tunnel phases between leads in each subsector, the $J_{jk}^{(\{\sigma\})}$ in Eq. (44) are real positive up to a global intersector phase $\varphi_{\mathcal{B}_1\mathcal{B}_2}^{(\{\sigma\})}$. Defining an effective tunneling amplitude between sectors $\mathcal{B}_1$ and $\mathcal{B}_2$ with the corresponding Pauli string $\{\sigma\}$,

$$J_{\mathcal{B}_1\mathcal{B}_2}^{(\{\sigma\})} = e^{i\varphi_{\mathcal{B}_1\mathcal{B}_2}^{(\{\sigma\})}}\sum_{j\in\mathcal{B}_1}\sum_{k\in\mathcal{B}_2} J_{jk}^{(\{\sigma\})}e^{i(\tilde{\varphi}_j-\tilde{\varphi}_k)}, \tag{45}$$

the intersector cotunneling Hamiltonian is given by

$$H_{\mathcal{B}_1\mathcal{B}_2} = J_{\mathcal{B}_1\mathcal{B}_2}^{(\{\sigma\})}\sigma^1\cdots\sigma^n e^{i(g_1\Phi_1-g_2\Phi_2)} + \text{H.c.} \tag{46}$$

The full strong-coupling tunneling Hamiltonian follows by summing over all subsector pairs. Several comments are now in order:

(i) The above discussion also holds if one of the subsectors $\mathcal{B}_{1,2}$ contains just a single lead, where Eq. (46) applies as soon as the other subsector enters strong coupling.

(ii) Phase differences between individual $\tilde{\varphi}_j$ (or $\tilde{\varphi}_k$) in Eq. (45) are pinned by the potential terms in Eq. (42). Therefore also the intersector differences $\tilde{\varphi}_j - \tilde{\varphi}_k$ are fixed, and all contributions to $J_{\mathcal{B}_1\mathcal{B}_2}^{(\{\sigma\})}$ in Eq. (45) add up with a collective intersector phase $\varphi_{\mathcal{B}_1\mathcal{B}_2}^{(\{\sigma\})}$.

(iii) Equation (46) implies a drastic reduction in the number of boson fields at strong coupling. However, the parameter g_0 in Eq. (41) implies that the collective fermionic lead obtained from ϕ_0 in general will represent an interacting fermion theory. To see this, we note that $\tilde{g} = 1/g_0^2 = M$ acts like a Luttinger liquid parameter [67,72]. For $M > 1$, we thus have attractive electron-electron interactions. We note in passing that RG couplings between isotropized subsectors acquire the same enhancement factor $\sim M = \tilde{g}$, see Sec. III and Ref. [67].

(iv) We may encounter multiple tunneling paths with distinct Pauli strings connecting both subsectors, in particular, for systems with closed loops. The strong-coupling Hamiltonian then contains a center-of-mass term as in Eq. (46) for each of these nonequivalent tunneling paths. Their relative phase,

$$\varphi^{\text{loop}} = \varphi_{\mathcal{B}_1\mathcal{B}_2}^{(\{\sigma\})} - \varphi_{\mathcal{B}_1\mathcal{B}_2}^{(\{\sigma'\})}, \tag{47}$$

coincides with the loop phase in Eq. (25).

We emphasize that the strong-coupling projection of bosonic subsectors to center-of-mass fields is not limited to a specific setup. In particular, the same idea allows one to elegantly discuss nonequilibrium effects due to applied bias voltages in simply-coupled systems [67], see also Appendix C. For the resulting effective models, similar to the discussion in Sec. III A, our approach only depends on whether tunneling paths between a pair of subsectors contain overall commuting or anticommuting Pauli strings. For mutually commuting operators, we arrive at RG equations as in Eqs. (20) and (21). Now consider two tunneling operators with couplings $J_{\mathcal{B}_1\mathcal{B}_2}^{(\{\sigma\})}$ and $J_{\mathcal{B}_2\mathcal{B}_3}^{(\{\sigma'\})}$, which connect subsector $\mathcal{B}_2$ with subsectors $\mathcal{B}_1$ and $\mathcal{B}_3$, respectively, cf. Appendix A. If the corresponding Pauli strings anticommute, no RG contributions will be generated for arbitrary couplings $J_{\mathcal{B}_1\mathcal{B}_3}^{(\{\sigma''\})}$ between $\mathcal{B}_1$ and $\mathcal{B}_3$. However, if two (or more) paths between a *pair* of subsectors contain anticommuting Pauli strings, one obtains the hybridization and feedback contributions discussed in Sec. III A.

B. Decoupling fields via hybridization terms

A second key ingredient concerns a decoupling of certain linear combinations of boson fields from cotunneling operators with Pauli strings. Such strategies go back to the work of Emery and Kivelson (EK) [79] and are often used for Kondo systems, see, e.g., Refs. [70,80,83]. In particular, they show that the relevant low-energy degrees of freedom at strong coupling usually differ from those at weak coupling. After an orthogonal rotation of the original set of lead boson fields $\{\phi_j(x)\}$ to a new set of boson fields $\{\phi_\alpha(x)\}$, which corresponds to a highly nonlocal operation in terms of the underlying fermions, one performs a unitary rotation involving Pauli operators and the boundary phase fields $\Phi_\alpha = \phi_\alpha(0)$. One can thereby trade off the coupling of some boson species with a Pauli operator in favor of a hybridization term. These generalized EK decoupling schemes can allow for exact results at special parameter choices (Toulouse points) [70], where the bare hybridization, cf. Sec. III, is precisely compensated by the effects of the unitary transformation.

1. Center-of-mass (charge) field decoupling

We first discuss this strategy for systems with near-degenerate box charge states described by a spin operator $\mathbf{S}_a$ for box a, see Eq. (10) and Sec. II C. This idea was discussed for the single-impurity TKE in Refs. [64,68,69].

For our more general systems with Pauli operators and several boson fields, our approach differs only in the type of fields that are decoupled. While for one near-degenerate box, one can decouple the center-of-mass ('charge') field [64,68,69], for two (or more) coupled near-degenerate boxes, one should first project to the combined lowest-energy charge state. For example, in the notation of Eq. (10), we have

$$H_{ab} \simeq \Delta E_a S_z^a + \Delta E_b S_z^b + \sum_{j,k} (t_{jk}\gamma_j\gamma_k S_{+,a}S_{-,b} + \text{H.c.}), \tag{48}$$

with MZMs $\gamma_{j/k}$ on box a/b, respectively. Note that the total interbox tunneling amplitude, $t_{ab} = \sum_{j,k} t_{jk}\gamma_j\gamma_k$, fluctuates as it depends on the Majorana parities $i\gamma_j\gamma_k = \pm 1$. For nearly charge-degenerate cases, we have $|t_{ab}| \gg \Delta E_{a/b} \sim \Delta n_{g,a/b}$, and one can project onto the subspace spanned by the lowest-energy total charge states, e.g., $|0\rangle_{ab} = |0_a 1_b\rangle$ and $|1\rangle_{ab} = |1_a 0_b\rangle$ in the notation of Sec. II C.

Using this strategy, one arrives at a single (or conglomerate of strongly coupled) box(es) attached only to leads on the outside. With total-charge states described by a collective spin variable $\mathbf{S}$, one finds a general tunneling Hamiltonian as in Eq. (10). Using the center-of-mass field Φ_0 and reduced fields $\tilde{\Phi}_k$ as in Sec. IV A, we obtain the boundary term, see also [64,69],

$$H_b = \sum_{j,k} (\lambda_{jk}\gamma_j\kappa_k S_+ e^{-i(\tilde{\Phi}_k + \frac{1}{\sqrt{M}}\Phi_0)} + \text{H.c.}) + \Delta E S_z, \tag{49}$$

where $\Delta E \sim \Delta n_g$ is the overall detuning energy between the total charge states $S_z = \pm 1/2$. We now notice that an EK-type unitary rotation, $U = e^{-i\frac{1}{\sqrt{M}}\Phi_0 S_z}$, can decouple the center-of-mass field Φ_0. The tunneling Hamiltonian, $\tilde{H}_b = U H_b U^\dagger$, is then of the form

$$\tilde{H}_b = \sum_{j,k} (\lambda_{jk}\gamma_j\kappa_k S_+ e^{-i\tilde{\Phi}_k} + \text{H.c.}) + (\Delta E - \Lambda\Theta_0')S_z, \tag{50}$$

where the term $\Lambda\Theta_0' S_z$ comes from the transformation of H_{leads}. Clearly, by tuning $\Delta E \sim \Delta n_g$, one could quench the last (hybridization) term in Eq. (50). The reduced field combinations $\tilde{\Phi}_k$ do not change the box charge state anymore due to the constraint $\sum_k \tilde{\Phi}_k = 0$. Rather these new fields describe injection of a single electron from lead k, which is then transmitted into all outer leads with the same probability. Together with the isotropization of the λ_{jk} couplings, this constitutes a hallmark for the TKE [64,69]. We therefore expect TKE physics to be ubiquitous in systems of coupled near-degenerate boxes.

2. *Relative (spin) field decoupling*

Following a similar strategy, we now give an example for how to decouple relative ('spin') fields in the cotunneling regime of charge-quantized coupled box systems. We focus on the single-MZM two-lead junction described by the junction Hamiltonian $H_{1,2}$ in Eq. (12), see Fig. 2(c) and Sec. II C, where the boson fields $\Phi_{x,y}$ refer to the two leads coupled to a single MZM.

We first switch to linear combinations of the lead bosons, $\phi_{c,s}(x) = (\phi_x(x) \pm \phi_y(x))/\sqrt{2}$, and analogously for the conjugate θ_ν fields. As shorthand, we will just write $\Phi_c = (\Phi_x + \Phi_y)/\sqrt{2}$ and $\Phi_s = (\Phi_x - \Phi_y)/\sqrt{2}$, with the implicit understanding that the transformation is also carried out in the bulk. From Eq. (12), we then obtain

$$H_{1,2} = (\lambda_x\sigma_x e^{i\frac{\Phi_s}{\sqrt{2}}} + \lambda_y\sigma_y e^{-i\frac{\Phi_s}{\sqrt{2}}})e^{i(\frac{\Phi_c}{\sqrt{2}} - \varphi)} + \text{H.c.}, \tag{51}$$

where only the Φ_s field couples in an essential manner to the Pauli operators $\sigma_{x,y}$.

At this point, we apply the unitary transformation $U = e^{i\sigma_z\Phi_s/\sqrt{2}}$. Switching to $\sigma_\pm = (\sigma_x \pm i\sigma_y)/2$, the transformed junction Hamiltonian, $\tilde{H}_{1,2} = U H_{1,2} U^\dagger$, is given by

$$\begin{aligned}\tilde{H}_{1,2} = {} & [\lambda_x(\sigma_+ + \sigma_- e^{\sqrt{2}i\Phi_s}) - i\lambda_y(\sigma_- + \sigma_+ e^{-\sqrt{2}i\Phi_s})] \\ & \times e^{i(\frac{\Phi_c}{\sqrt{2}} - \varphi)} + \text{H.c.}\end{aligned} \tag{52}$$

In addition, transformation of the lead Hamiltonian generates a hybridization term $(v_F/\sqrt{2})\sigma_z\Theta_s'$. The $\lambda_{x/y}$ terms now contain rapidly oscillating phase exponentials of Φ_s. In the spirit of the rotating-wave approximation, we drop such highly irrelevant tunneling operators. We then obtain the boundary Hamiltonian

$$\tilde{H}_b = (\lambda_x\sigma_+ - i\lambda_y\sigma_-)e^{i(\frac{\Phi_c}{\sqrt{2}} - \varphi)} + \text{H.c.} + \Lambda\sigma_z\Theta_s', \tag{53}$$

where Λ includes a bare coupling value and the above $v_F/\sqrt{2}$ term. The field Φ_s has thus been decoupled at the cost of an interaction between the lead density $\sim\Theta_s'$ and the Pauli operator σ_z. However, at the special Toulouse point, $\Lambda = 0$, the spin-field combination disappears completely. We note that for the example discussed here, an equivalent decoupling can also be achieved with a fermionic representation of the leads. In the remainder of this section, see also Sec. V, we employ the above ideas to study the strong-coupling regime for the applications discussed from the weak-coupling RG perspective in Secs. III B–III D.

C. Two-box device

For the two-box device in Fig. 3, see Sec. III B, according to our strategy in Sec. IV A, we first identify the important boson fields that should be kept in the strong-coupling analysis. There are four such fields, namely the center-of-mass fields for the left/right box, $\Phi_{L/R}$, with $g_{L/R} = 1/\sqrt{M_{L/R}}$ in Eq. (41), and the left/right central lead fields, $\Phi_{l/r}$, with $g_{l/r} = 1$. We then have five different intersector couplings: $J_Z, J_{X,l/r}$, and $J_{Y,r/l}$. Since those effective couplings are obtained by summing over individual leads, they include enhancement factors $\sim M_{L,R}$, cf. Sec. IV A. From the cotunneling Hamiltonian in Eqs. (27) and (28), the effective strong-coupling theory follows as

$$H_{\text{eff}} = \sum_{\nu=L,R,l,r} H_{\text{leads}}[\phi_\nu,\theta_\nu] - \frac{1}{2}(\Gamma_b + \Gamma_b^\dagger), \tag{54}$$

with the boundary operator

$$\begin{aligned}\Gamma_b = {} & J_{X,l}\sigma_x e^{i(\Phi_l - g_L\Phi_L)} + J_{X,r}\sigma_x e^{i(\Phi_r - g_R\Phi_R)} \\ & + J_{Y,l}\sigma_y e^{i(\Phi_l - g_R\Phi_R)} + J_{Y,r}\sigma_y e^{i(\Phi_r - g_L\Phi_L)} \\ & + iJ_Z\sigma_z e^{i(g_L\Phi_L - g_R\Phi_R)}.\end{aligned} \tag{55}$$

For arbitrary device parameters, further analytical progress is difficult even though always at least one of the charge/spin combinations of the central lead fields, $\Phi_{c,s} = (\Phi_l \pm \Phi_r)/\sqrt{2}$, can be decoupled by an EK transformation, see Sec. IV B. For instance, when studying transport between L/R leads, a decoupling of Φ_s is most sensible. In any case, numerical approaches can provide another option to investigate the physics encoded by Eq. (55), e.g., via quantum Monte Carlo simulations [85] or the numerical renormalization group [59].

We here instead focus on a simpler yet nontrivial two-box setup which does allow for analytical progress. Such a device is shown in Fig. 1, where in contrast to the case depicted in Fig. 3, we now only have a single central lead (Φ_l). The strong-coupling Hamiltonian for this device follows directly from Eqs. (54) and (55) by putting $J_{X/Y,r} = 0$. The remaining couplings are given by

$$J_x = J_{X,l}, \quad J_y = J_{Y,l}, \quad J_z = J_Z. \tag{56}$$

We then perform an EK transformation with $U = e^{i\sigma_z(\Phi_l - g_R\Phi_R)}$. Following the steps in Sec. IV B, the transformed Hamiltonian, $\tilde{H}_{\rm eff} = H_{\rm leads} + \tilde{H}_b$, contains the boundary term

$$\begin{aligned}\tilde{H}_b &= -\tfrac{1}{2}(\tilde{\Gamma}_b + \tilde{\Gamma}_b^\dagger) + \Lambda\sigma_z(\Theta_l' - g_R\Theta_R'),\\ \tilde{\Gamma}_b &= (J_x\sigma_+ - iJ_z\sigma_z)e^{-i(g_L\Phi_L - g_R\Phi_R)} - iJ_y\sigma_+.\end{aligned} \tag{57}$$

The hybridization parameter $\Lambda = \Lambda_0 - v_F$ includes a bare coupling Λ_0, where v_F is due to the EK transformation of $H_{\rm leads}$. Next, we perform an orthogonal rotation of the $\phi_{L/R}(x)$ phase fields,

$$\begin{pmatrix}\phi_1\\ \phi_2\end{pmatrix} = \frac{1}{\bar{g}}\begin{pmatrix}g_L & -g_R\\ g_R & g_L\end{pmatrix}\begin{pmatrix}\phi_L\\ \phi_R\end{pmatrix}, \quad \bar{g} = \sqrt{g_L^2 + g_R^2}, \tag{58}$$

resulting in

$$\begin{aligned}\tilde{H}_b = &-\frac{1}{2}((J_x\sigma_+ - iJ_z\sigma_z)e^{-i\bar{g}\Phi_1} + \text{H.c.} + J_y\sigma_y)\\ &+ \frac{\Lambda}{\bar{g}}\sigma_z\big(\bar{g}\Theta_l' + g_R^2\Theta_1' + g_Rg_L\Theta_2'\big).\end{aligned} \tag{59}$$

The setup with $M_L = M_R = 2$ in Fig. 1 now gives access to an exact solution at the Toulouse point, $\Lambda = 0$, via the refermionization approach [70]. Indeed, for $\bar{g} = 1$, which only holds for $M_L = M_R = 2$, the operator $e^{-i\bar{g}\Phi_1}$ in Eq. (59) can be expressed as fermion annihilation operator (up to a Klein factor), and $\tilde{H}_{\rm eff}$ thus reduces to a noninteracting fermion theory for $\Lambda = 0$. In the remainder of this subsection, we thus assume $M_L = M_R = 2$ as in Fig. 1, but for now still allow for $\Lambda \neq 0$.

At this stage, we employ Eq. (5) backwards to obtain chiral fermion operators $\psi_\nu(x)$ associated with the respective boson field ϕ_ν with mode index $\nu = 1,2,l$. Using $\Psi_\nu = \psi_\nu(0)$ and recalling that $\Psi_\nu^\dagger \sim \kappa_\nu e^{i\Phi_\nu}$, see Eq. (5), Klein factors (κ_ν) are again represented as Majorana operators. In addition, we express Pauli operators as Majorana bilinears, $\sigma_{\alpha=x,y,z} = i\gamma_\alpha\gamma_0$, with the overall parity constraint $\gamma_0\gamma_x\gamma_y\gamma_z = 1$. We now notice (i) that $\kappa_{\nu=1}$ is the only Klein factor which explicitly appears in $\tilde{H}_{\rm eff}$, and (ii) that $i\gamma_0\kappa_1 = \pm 1$ is conserved. Choosing $i\gamma_0\kappa_1 = -1$, Eq. (59) yields

$$\begin{aligned}\tilde{H}_b = &J_x\gamma_x(\Psi_1^\dagger - \Psi_1) + i(J_x\gamma_y - J_z\gamma_z)(\Psi_1^\dagger + \Psi_1)\\ &- \frac{iJ_y}{2}\gamma_z\gamma_x + i\Lambda\gamma_y\gamma_x : 2\Psi_l^\dagger\Psi_l + \Psi_1^\dagger\Psi_1 - \Psi_2^\dagger\Psi_2 : ,\end{aligned} \tag{60}$$

where : : indicates normal-ordering and $1/\sqrt{\alpha}$ factors from the short-distance cutoff in Eq. (5) have been absorbed in $J_{x,z}$. Clearly, in the Toulouse limit, we indeed have noninteracting fermions. In the final step, we switch to chiral Majorana fermions by writing

$$\psi_\nu(x) = [\xi_\nu(x) + i\eta_\nu(x)]/\sqrt{2}, \tag{61}$$

where $\xi_\nu(x) = \xi_\nu^\dagger(x)$ and $\eta_\nu(x) = \eta_\nu^\dagger(x)$ obey the algebra $\{\xi_\nu(x),\eta_{\nu'}(x')\} = \delta(x - x')\delta_{\nu\nu'}$ and so on [70]. The bulk Hamiltonian then takes the form

$$H_{\rm leads} = -\frac{iv_F}{2}\sum_\nu \int_{-\infty}^{\infty} dx(\xi_\nu\partial_x\xi_\nu + \eta_\nu\partial_x\eta_\nu), \tag{62}$$

and the Toulouse Hamiltonian is given by

$$\begin{aligned}H_{\rm Toul} = &H_{\rm leads} - i\sqrt{2}J_x\gamma_x\eta_1(0)\\ &+ i\sqrt{2}(J_x\gamma_y - J_z\gamma_z)\xi_1(0) - \frac{iJ_y}{2}\gamma_z\gamma_x.\end{aligned} \tag{63}$$

Interaction corrections come from the Λ term in Eq. (60),

$$H_\Lambda = i\sum_{\nu=1,2,l}\Lambda_\nu\gamma_y\gamma_x\xi_\nu(0)\eta_\nu(0), \tag{64}$$

with couplings $\Lambda_\nu \sim \Lambda$. The corrections are RG irrelevant. In fact, for $J_{x,y,z} \neq 0$, they have scaling dimension $d_{\nu=l,2} = 3$ and $d_{\nu=1} = 2$, respectively. Finally, noting that $\Psi_1 \sim e^{-i\Phi_1} = e^{-i(\Phi_L - \Phi_R)/\sqrt{2}}$, we observe that the central lead (Ψ_l) decouples at the Toulouse point, i.e., no current will flow through this lead. A detailed discussion of nonequilibrium transport for this setup is given in Sec. V.

D. Single MZM coupled to multiple leads

Our next example is that of a single MZM coupled to two or three leads, see Sec. III C. Recall that this case derives from the two-box setting by taking $M = M_L$ leads connected by simple lead-MZM contacts, while $M_R = 1$ for the right box (boson field Φ_z). In addition, we have two central leads ($\Phi_{x,y}$). With the effectively isotropic Hamiltonian in Eq. (34), the construction of the strong-coupling theory then proceeds precisely as in Sec. IV C. In fact, $H_{\rm eff}$ follows directly by setting $M_R = 1$ in Eq. (55). Using the center-of-mass field $\Phi_L = g_L\sum_{j=1}^M \Phi_j$ with $g_L = 1/\sqrt{M}$, Eq. (54) holds with

$$\Gamma_b = \sum_{\alpha=x,y,z} J_\alpha\sigma_\alpha e^{i(g_L\Phi_L - \Phi_\alpha)}, \tag{65}$$

where the couplings J_α have been specified in Eq. (33).

This strong-coupling Hamiltonian again represents an interacting problem. However, for $J_z = 0$, analytical progress can be made by using the charge/spin fields $\Phi_{c,s}$ instead of $\Phi_{x,y}$. As discussed in Sec. IV B, the EK transformation $U = e^{i\sigma_z\Phi_s/\sqrt{2}}$ decouples Φ_s from Γ_b and generates a hybridization term from $H_{\rm leads}$. Moreover, by an orthogonal rotation $(\phi_L,\phi_c) \to (\phi_a,\phi_0)$, cf. Eq. (58), we switch to the linear combinations

$$\phi_a = \frac{1}{g_a}\left(g_L\phi_L - \frac{1}{\sqrt{2}}\phi_c\right),$$
$$\phi_0 = \frac{1}{\sqrt{M+2}}\left(\phi_x + \phi_y + \sum_{j=1}^{M}\phi_j\right), \tag{66}$$

with the parameter

$$g_a = \sqrt{g_L^2 + 1/2} = \sqrt{\frac{M+2}{2M}}. \tag{67}$$

The field ϕ_0 is nothing but the total center-of-mass phase field for all $M+2$ leads, which decouples from the transport problem. We hence obtain

$$\tilde{H}_{\rm eff} = \sum_{\nu=a,s} H_{\rm leads}[\phi_\nu,\theta_\nu] - \frac{1}{2}(\tilde{\Gamma}_b + \tilde{\Gamma}_b^\dagger) + \Lambda_s\sigma_z\Theta_s',$$
$$\tilde{\Gamma}_b = (J_x\sigma_+ + iJ_y\sigma_-)e^{ig_a\Phi_a}. \tag{68}$$

This Hamiltonian describes collective charge transport between the M outer leads and the charge field $\Phi_c = (\Phi_x + \Phi_y)/\sqrt{2}$, where the Pauli operators $\sigma_{x,y}$ couple only to Φ_a, cf. Eq. (66). We find $\Lambda_s = \Lambda_0 - v_F/\sqrt{2}$ with the bare hybridization Λ_0.

In general, this is an interacting theory even at the Toulouse point, $\Lambda_s = 0$. Indeed, refermionization of the ϕ_a channel implies attractive electron-electron interactions since $\tilde{g}_a = 1/g_a^2 > 1$ for $M > 2$, see Eq. (67). The only exception to this rule arises for $M = 2$, where $g_a = 1$ and refermionization obtains a noninteracting fermion theory for $\Lambda_s = 0$. We thus put $M = 2$ and refermionize the two remaining lead channels $\nu = a,s$ as in Sec. IV C. In addition, we again write Pauli operators as bilinears of Majorana operators, $\sigma_{\alpha=x,y,z} = i\gamma_\alpha\gamma_0$, with $\gamma_0\gamma_x\gamma_y\gamma_z = 1$. Using the fermion operator $d = (\gamma_x + i\gamma_y)/2$, we thus have

$$\sigma_+ = \sigma_-^\dagger = id\gamma_0, \quad \sigma_z = 1 - 2d^\dagger d, \tag{69}$$

and the tunneling operator $\tilde{\Gamma}_b$ in Eq. (68) has the form

$$\tilde{\Gamma}_b = i\gamma_0\kappa_a(J_x d + iJ_y d^\dagger)\Psi_a^\dagger, \tag{70}$$

where the cutoff in Eq. (5) has been absorbed in $J_{x,y}$. Clearly, the local parity $i\gamma_0\kappa_a$ is conserved. Choosing $i\gamma_0\kappa_a = +1$, we get the boundary contribution to $\tilde{H}_{\rm eff} = H_{\rm leads} + \tilde{H}_b$ in the form

$$\tilde{H}_b = -\frac{1}{2}J_x(\Psi_a^\dagger d + d^\dagger\Psi_a) - \frac{i}{2}J_y(\Psi_a^\dagger d^\dagger - d\Psi_a)$$
$$- \Lambda_s\big(2d^\dagger d - 1\big) : \Psi_s^\dagger\Psi_s : \tag{71}$$

Using $J_\pm = (J_y \pm J_x)/2\sqrt{2}$ and the chiral Majorana fermion representation in Eq. (61), we can alternatively write

$$\tilde{H}_b = iJ_+\xi_a(0)\gamma_x + iJ_-\eta_a(0)\gamma_y + \Lambda_s\gamma_x\gamma_y\xi_s(0)\eta_s(0). \tag{72}$$

Remarkably, the just obtained effective strong-coupling Hamiltonian $\tilde{H}_{\rm eff}$ for the setup in Fig. 1 coincides with the asymmetric two-channel Kondo model studied in detail in Ref. [80]. Let us briefly summarize the corresponding physics. First, in the channel-symmetric case, $J_- = 0$, the system shows non-Fermi liquid behavior at the Toulouse point, $\Lambda_s = 0$. The leading irrelevant operator $\sim\Lambda_s$ has scaling dimension $d = 3/2$ which determines the power-law exponent of the temperature- and/or voltage-dependent conductance [70]. For $J_- \neq 0$, on the other hand, the Toulouse Hamiltonian obtained from Eq. (72) is a sum of two independent Majorana resonant level models and thus exhibits Fermi liquid behavior at low energy scales. Furthermore, at the Toulouse point but otherwise for arbitrary $J_\pm$, exact results for the full counting statistics of nonequilibrium transport have been derived by Gogolin and Komnik [81]. Their results immediately apply to the present setting, see also Sec. V.

E. Loop qubit

Last we turn to the strong-coupling regime of the loop qubit device depicted in Fig. 4. While a limiting case of the problem, cf. Eq. (73) below, has already been addressed in Ref. [63], in view of the present experimental interest in this device, we here give a more complete picture. Following the strategy in Sec. IV A, we first define a center-of-mass field for the M outer leads, $\Phi_L = g_L\sum_{j=1}^M \Phi_j$ with $g_L = 1/\sqrt{M}$. We also recall that Φ_c denotes the boson field for the central lead contacting two MZMs on the box, see Fig. 4. Our weak-coupling analysis in Sec. III D has then identified two qualitatively different candidate strong-coupling fixed points.

The first type is stable and describes an RG flow towards loop phase $\varphi_0 = \pm\pi/2$. Without loss of generality, we choose $\varphi_0 = +\pi/2$, where one has a strong complex-valued cotunneling amplitude L_+ and a vanishing amplitude L_- in Eq. (37). We then obtain the strong-coupling theory, $H_{\rm eff} = H_{\rm leads} + H_{\varphi_0=\pi/2}$, with

$$H_{\varphi_0=\pi/2} = -J_+\sigma_+e^{i(g_L\Phi_L - \Phi_c)} + \text{H.c.} + \Lambda\sigma_z\Theta_c', \tag{73}$$

where $J_+ = ML_+/\sqrt{2}$ and $\Lambda = 2(\Lambda_c - \tilde{\Lambda})$, see Sec. III D. For $M = 1$, Ref. [63] found that this model can be mapped onto a fully anisotropic single-channel Kondo model. For $M \geqslant 2$, as we discuss below, the central lead Φ_c instead dynamically decouples from the outer leads which in turn develop a TKE for $M \geqslant 3$.

The second fixed point, taken as $\varphi_0 = 0$ without loss of generality, is unstable with respect to phase variations $\delta\varphi_0$, see Sec. III D. This fixed point is qualitatively different from the first one, as it implies $L_+ = L_-$ and $\Lambda \sim \sin\varphi_0 = 0$. The strong-coupling theory follows from Eqs. (36) and (37),

$$H_{\varphi_0=0} = -(J_x\sigma_x + J_y\sigma_y)e^{i(g_L\Phi_L - \Phi_c)} + \text{H.c.} \tag{74}$$

with $J_{x,y} \sim \lambda_{x,y}$ in Eq. (36). Next we use the local fermion parity representation of Pauli operators, $\sigma_{x,y} = i\gamma_{x,y}\kappa$. Since both J_x and J_y are real, with fixed ratio during the RG flow, we can construct a new Majorana operator

$$\gamma = (J_x\gamma_x + J_y\gamma_y)/J, \quad J = \sqrt{J_x^2 + J_y^2}. \tag{75}$$

The central contact thus couples to a single Majorana operator γ only, since the relative tunneling phase between the lead and the two original MZMs is zero (or π). For other values of φ_0, such a reduction is not possible. However, the above reasoning is not restricted to the cotunneling regime. The same steps also apply for the tunneling Hamiltonian in Eq. (36), and hence we expect this effect to always appear so long as $\varphi_0 = 0 \bmod \pi$.

Finally, we note that Eq. (74) has conserved fermion parity $i\gamma\kappa = \pm 1$. Choosing $i\gamma\kappa = 1$, we obtain

$$H_{\varphi_0=0} = -2J\cos(g_L\Phi_L - \Phi_c). \tag{76}$$

Using the results of Ref. [67], where Eq. (76) also appears, we thus have access to the full nonequilibrium transport characteristics between the central lead and an arbitrary number $M \geqslant 2$ of outer leads.

The loop qubit device in Fig. 4 is likely most relevant as a starting point to more complicated Majorana multijunctions and networks. To guide such experimental tests, let us briefly summarize how quantum transport is expected to depend on the loop phase φ_0. First, since experiments are performed at small but finite temperature and bias, features of the unstable fixed point should appear in a region around $\varphi_0 = 0 \bmod \pi$ with small but nonzero hybridization. Now consider the case $M = 1$. If $\varphi_0 \approx 0$, our theory predicts qualitatively the same behavior as for a two-terminal mesoscopic Majorana wire [45–47]. While transport for half-integer n_g, i.e., at a charge-degeneracy point, exhibits the quantized zero-temperature conductance $G_0 = e^2/h$, transport in the cotunneling regime will be strongly suppressed. Conversely, as one increases φ_0, the conductance should approach G_0 largely independent of n_g. Tunneling of charges then is not due to charge-degenerate states but rather caused by a Kondo resonance [63]. The latter arises due to many-body screening of the spin-1/2 impurity $\sim (\sigma_x,\sigma_y,\sigma_z)$ built from three Majorana operators, two at the central and one at the simply-coupled lead. Next we consider the case $M \geqslant 2$, i.e., a multiterminal measurement of conductance between the central lead and outer leads in Fig. 4. Starting again with $\varphi_0 \approx 0$, the device should display the transport behavior expected for the TKE [53–57,67], with fractional conductance values at zero temperature and non-Fermi liquid power laws in the temperature- and/or voltage-dependent conductance. In the loop qubit device, a natural experiment includes probing the finite-bias conductance through the central lead, which for $\varphi_0 \approx 0$ should reveal the features discussed in Ref. [67]. For increasing φ_0, the ensuing hybridization Λ at the central (and all other) leads will gap out the Majorana fermion pair involved in $\sigma_z = i\gamma_y\gamma_x$. As a consequence, transport involving the central lead will be blocked at temperatures and/or voltages below the Kondo temperature T_K of the box. We thus predict drastically different low-energy conductance behavior depending on both the loop phase φ_0 and on the number of attached leads.

Finally, tuning the system to near half-integer n_g is not expected to qualitatively affect the above conclusions for $M \geqslant 2$, cf. Secs. II C and IV B. However, the Kondo temperature is expected to strongly depend on n_g [64,69]. Therefore, while the approach to a universal conductance value in the strong-coupling regime takes place independent of the loop phase $\varphi_0 \neq 0$ and of the gate parameter n_g, the finite-energy behavior will depend on those parameters.

V. TRANSPORT IN A TWO-BOX DEVICE

In this section, we study nonequilibrium transport properties for the two-box device in Fig. 1 by employing the strong-coupling theory in Sec. IV C. We consider the system right at the Toulouse point, with the noninteracting Hamiltonian $H_{\rm Toul}$ in Eq. (63). The resulting physics is expected to be generic since interaction corrections around the Toulouse point, see Eq. (64), are RG irrelevant. For closely related models, an exact solution for the full counting statistics of charge transport has been described in Refs. [81,83]. In what follows, we adapt those results to the setup in Fig. 1.

To that end, we first recall that at the Toulouse point, the central lead ψ_l will dynamically decouple from the transport problem, see Sec. IV C. However, a small residual current is expected to flow through the central lead due to RG irrelevant interaction corrections not considered below. We thus focus on a transport configuration, where the $M_L = 2$ ($M_R = 2$) leads attached via simple contacts to the left (right) box are held at chemical potential $+eV/2$ ($-eV/2$). In particular, there are no applied voltages between leads attached to the same box. If the latter were present, quick equilibration of leads at each box is expected due to the large intrasector coupling. In contrast, the interbox coupling may be small and equilibration is perturbed by the central nonsimple junction. We then consider the outcome of a two-terminal measurement of the fluctuating time-dependent current, $I(t)$, flowing between individual pairs of leads on different sides. (The relation to collective intersector transport is discussed below and in Appendix C.) During a measurement time t_m, the charge $q = \int_0^{t_m} dt' I(t')/e$ is transferred between the two leads, where the full counting statistics of q follows from a cumulant generating function $\chi(\lambda)$. In particular, by taking derivatives with respect to the counting field λ, one obtains all cumulants from the relation $\langle \delta^n q\rangle = (-i)^n \partial_\lambda^n \ln\chi(\lambda = 0)$. Below we only discuss the average current I and the current noise S, which are given by

$$I = \frac{e}{t_m}\langle \delta q\rangle, \quad S = \frac{2e^2}{t_m}\langle \delta^2 q\rangle. \tag{77}$$

We next relate transport between individual leads attached to the left and right box, respectively, to the transformed fermion basis at strong coupling, cf. Sec. IV C. To this end, observe that application of the operator $\Psi_1 \sim e^{-i(\Phi_L - \Phi_R)/\sqrt{2}}$ on an arbitrary system state amounts to transporting one unit of charge between the left and right side. Recalling the center-of-mass phases $\Phi_L = (\Phi_{L_1} + \Phi_{L_2})\sqrt{2}$ and $\Phi_R = (\Phi_{R_1} + \Phi_{R_2})\sqrt{2}$ in terms of the physical leads $L_{1,2}$ and $R_{1,2}$, per tunneling event, the charge transferred at each individual lead hence is $e^* = e/2$. One thus can include the counting field by letting $\Psi_1 \to e^{+(-)i\lambda/4}\Psi_1$ on the forward (backward) time branch of the Keldysh partition function for $H_{\rm Toul}$ [81]. Since the projected theory in Eq. (63) contains only Ψ_1, the inclusion of a counting field is relevant only for one out of the four fermion species in the ensuing two-channel Kondo model [83].

After some algebra along the steps in Refs. [81,83], where only the Green's functions for the three impurity-Majorana operators $\gamma_{x,y,z}$ in Eq. (63) have to be updated, we obtain the zero-temperature generating function,

$$\ln\chi(\lambda) = \frac{t_m}{2\pi}\int_0^{eV/2} d\omega \ln(1 + \mathcal{T}(\omega)[e^{i\lambda} - 1]), \tag{78}$$

with the frequency-dependent transparency

$$\mathcal{T}(\omega) = \frac{\left(\Gamma_z\omega^2 - \Gamma_x J_y^2\right)^2}{\left(\Gamma_x^2 + \omega^2\right)\left[\left(\omega^2 - J_y^2\right)^2 + \omega^2(\Gamma_x + \Gamma_z)^2\right]}. \tag{79}$$

We here define the energy scales $\Gamma_{x,z} \sim J_{x,z}^2$, where the proportionality constant also takes into account the rescaling of $J_{x,z}$ due to the short-distance cutoff in Eq. (5), see Sec. IV C. We mention in passing that the finite-temperature variant of Eq. (78) can readily be expressed in terms of Eq. (79) as well, cf. Refs. [81,83]. Let us then discuss the predictions of Eq. (78) for the current-voltage characteristics and for shot noise in this system.

A. No Majorana hybridization: $J_y = 0$

We start with the case $J_y = 0$, where the MZM operators γ_x and γ_z are not hybridized. Defining the channel hybridizations

$$\Gamma_1 = \Gamma_x, \quad \Gamma_2 = \Gamma_x + \Gamma_z, \tag{80}$$

Eq. (79) takes the simpler form

$$\mathcal{T}_{J_y=0}(\omega) = \frac{(\Gamma_1 - \Gamma_2)^2\omega^2}{(\omega^2+\Gamma_1^2)(\omega^2+\Gamma_2^2)}. \tag{81}$$

Equation (81) gives the transparency of two competing Majorana channels coupled by the respective channel hybridization $\Gamma_{1,2}$ to a single impurity and therefore describes the asymmetric two-channel Kondo effect [80,83]. In fact, after a rotation of the impurity-Majorana sector, $H_{\rm Toul}$ in Eq. (63) directly corresponds to the Hamiltonian in Eq. (72), with $\Gamma_{1/2} = \Gamma_{-/+} \sim J_{-/+}^2$. The current-voltage characteristics readily follow from Eqs. (77)–(81),

$$I = \frac{e}{h}\frac{\Gamma_2 - \Gamma_1}{\Gamma_2 + \Gamma_1}\left[\Gamma_2 \tan^{-1}\left(\frac{eV}{2\Gamma_2}\right) - \Gamma_1 \tan^{-1}\left(\frac{eV}{2\Gamma_1}\right)\right]. \tag{82}$$

It is instructive to consider several limiting cases of Eq. (82).

First, the current (82) between the left and the right side vanishes identically for the channel-symmetric case with $\Gamma_2 - \Gamma_1 = \Gamma_z \to 0$. In fact, this result makes sense because the dependence of Γ_z on the microscopic tunnel amplitudes implies that both boxes are decoupled in that limit, $\sqrt{\Gamma_z} \sim J_z \sim \lambda_L\lambda_R t_{LR}/E_C^2 \to 0$.

Second, a related observation is that by increasing Γ_x at a fixed value of Γ_z, the current in Eq. (82) will also decrease. Indeed, for $\Gamma_x/\Gamma_z \to \infty$, Eq. (80) implies that we effectively come back to the limit $\Gamma_1 = \Gamma_2$ again, where the current vanishes. We note that in order to increase $\sqrt{\Gamma_x} \sim J_x \sim \lambda_L\lambda_l/E_C$ at fixed Γ_z, the tunnel coupling λ_l between the left box and the central lead has to increase. Although charge transfer at the central contact is dynamically blocked, the coupling Γ_x still has profound effects on the system. In particular, for $\Gamma_x \neq 0$, the central junction is effectively driven out of resonance by a misalignment of the spin direction $\sim(\sigma_x,\sigma_y,\sigma_z)$ with respect to the left-right transport direction $\sim\Gamma_z$.

Finally, in the opposite limit $\Gamma_x/\Gamma_z \to 0$, we instead approach the single-channel case with transparency

$$\mathcal{T}_{\Gamma_x=J_y=0}(\omega) = \frac{\Gamma_z^2}{\omega^2+\Gamma_z^2}, \tag{83}$$

where we note that $\Gamma_1 = \Gamma_x = 0$ in Eq. (80) implies $\Gamma_2 = \Gamma_z$. From Eq. (77), we obtain for $(eV,\Gamma_x) \ll \Gamma_z$ the transport observables

$$I = \frac{e}{2h}\left[eV - 2\Gamma_x \tan^{-1}\left(\frac{eV}{2\Gamma_x}\right)\right],$$
$$S = \frac{2e^2}{h}\left[\frac{\Gamma_x}{2}\tan^{-1}\left(\frac{eV}{2\Gamma_x}\right) - \frac{\Gamma_x^2}{(eV)^2+4\Gamma_x^2}eV\right]. \tag{84}$$

Defining the backscattered current $I_b = (e^2/2h)V - I$, we see that for $\Gamma_x \ll eV \ll \Gamma_z$, the shot noise power is given by $S = 2e^* I_b$ with elementary charge $e^* = e/2$. The shot noise comes from the weakly coupled (Γ_1) channel, while the strongly coupled (Γ_2) channel is fully transmitted (with the two-channel Kondo value of the conductance, $G = e^2/2h$) and thus noiseless. Equation (84) yields the same fractional Fano factor, $F = S/2I_b = e^*/e = 1/2$, as recently found in a related two-channel charge Kondo system [83]. In our case, a single additional Majorana operator enters the low-energy theory for $\Gamma_x > 0$, given by the Klein factor κ_l at the central lead, see Fig. 1. In the Toulouse-point Hamiltonian $H_{\rm Toul}$ in Eq. (63) it is represented by the Majorana operator γ_x. This causes the backscattering processes in Eq. (84), described by the fractional charge $e^* = e/2$.

For $\Gamma_x \to 0$, we also can draw an interesting link to the single-impurity TKE. Indeed, since the left and right boxes are now joined by a strong coupling Γ_z, this two-box setup should be related to the TKE for a single large box with $M = M_L + M_R = 4$ attached leads, cf. Sec. III B. Taking into account results by Béri [67], we offer a detailed discussion of this correspondence in Appendix C. The subsector-biased case considered here, with applied voltage $V_{L,R} = \pm V/2$ for all leads with $j \in \mathcal{B}_L$ and $k \in \mathcal{B}_R$, respectively, is slightly more involved than the one in Ref. [67]. For the two-terminal conductance measurement in Eq. (84), we here find $G_{jk} = e^2/2h$ between any pair of individual leads j and k. Instead, for collective intersector transport, we show in Appendix C that the left-right conductance is given by $G_{LR} = 2e^2/h$. The latter arises by summing the current over all leads in the respective subsectors, and it comprises cross-correlated Andreev reflections involving the Cooper pair charge $e_{LR}^* = 2e$. The generation of these processes is detailed in Fig. 6 and Appendix C. We thus predict the appearance of different effective charges due to hybridization with the central lead ($e^* = e/2$) and due to finite-energy corrections in collective left-right intersector transport ($e_{LR}^* = 2e$).

B. Finite Majorana hybridization

Next we include the effects of a finite Majorana hybridization $J_y \neq 0$. In order to obtain a qualitative understanding, we first analyze the limit $J_y \gg \max(\Gamma_{x,z}, eV)$, where the impurity term $-i(J_y/2)\gamma_z\gamma_x$ in $H_{\rm Toul}$ implies the fixed parity $i\gamma_z\gamma_x = +1$. Equation (63) can therefore be projected to a simpler single-channel model, $H'_{\rm Toul} = H_{\rm leads} + i\sqrt{2}J_x\gamma_y\xi_1(0)$, where a single MZM ($\gamma_y$) is coupled to a single chiral Majorana mode (ξ_1). The parity constraint $i\gamma_z\gamma_x = +1$ here effectively blocks the other chiral Majorana channel $\sim\eta_1$. Indeed, for $J_y \to \infty$, the general transparency expression in Eq. (79) reduces to the single-channel result

$$\mathcal{T}_{J_y\to\infty}(\omega) = \frac{\Gamma_x^2}{\omega^2+\Gamma_x^2}, \tag{85}$$

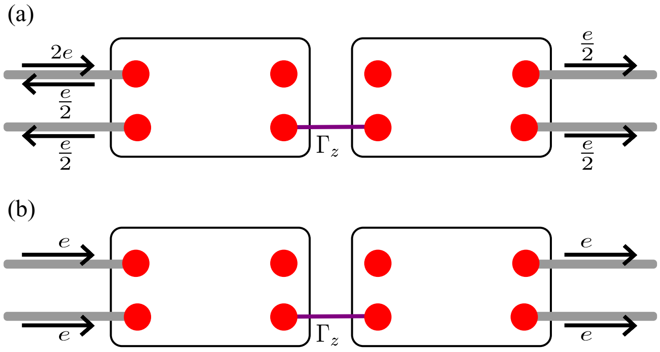

FIG. 6. Cross-correlated Andreev reflections (AR) generated from individual correlated AR processes in the two-box device with $J_y = 0$ and $\Gamma_x \to 0$, see Sec. V A. (a) A single AR at the top left lead, followed by the emission of charge $e/2$ into all four leads, forms a correlated AR process as in the TKE [54–56]. Since formation of charge dipoles between the left leads is suppressed by the strong intrasector coupling, a nonequilibrium excitation is left behind. (b) A sequence of two correlated ARs, one each at the top and bottom left leads, comprises a cross-correlated AR. This allows for the cotunneling of a Cooper pair by subsequent crossed ARs between left (in) and right (out) leads. For further discussion, see the main text and Appendix C.

but with active channel $\sim\Gamma_x$ instead of Γ_z in Eq. (83). We thus come back to single-channel results for conductance and shot noise again, with Γ_x as the only remaining parameter. Left-right transport then takes place exclusively by cotunneling via the central lead l in Fig. 1.

We next discuss the voltage dependence of the nonlinear conductance $G = I/V$, which is plotted for typical parameters in Fig. 7. The shown curves have been obtained by numerical evaluation of Eqs. (77)–(79). First, the conductance for $\Gamma_1 = J_y = 0$ (black solid curve) illustrates the single-channel case in Sec. V A, where Eq. (84) gives $G = e^2/2h$ for $eV \ll \Gamma_2$, in accordance with Fig. 7. Second, turning to $\Gamma_1 \ll \Gamma_2$ but still keeping $J_y = 0$ (dashed green curve, with $\Gamma_1/\Gamma_2 = 0.001$), we

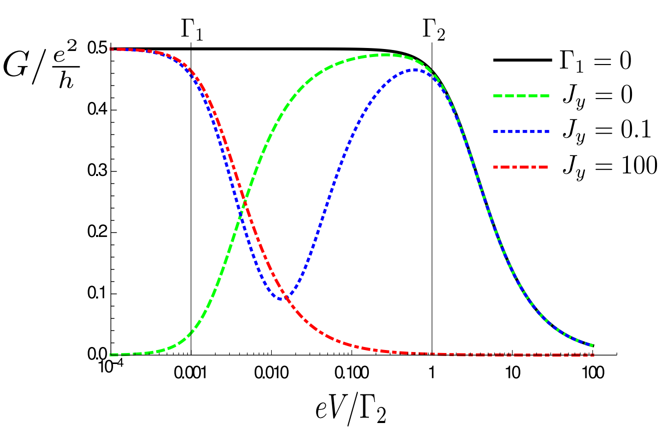

FIG. 7. Two-terminal conductance $G = I/V$ vs voltage V between two leads attached to different boxes in the two-box device of Fig. 1. The shown results hold at the Toulouse point, see Eq. (63), and follow from Eqs. (77)–(79). For detailed discussion, see the main text.

observe that the conductance vanishes at very low voltages but recovers to a large value near $e^2/2h$ within the window $\Gamma_1 \ll eV \ll \Gamma_2$. Such a behavior is consistent with our analytical result in Eq. (82), which describes the asymmetric two-channel Kondo effect with two competing Majorana channels coupled to an impurity.

The remaining two curves in Fig. 7 include the effects of a finite Majorana hybridization J_y, which now can cause antiresonances or resonances in the voltage dependence of the conductance. First, for $J_y \gg \max(\Gamma_{1,2}, eV)$, cf. the red dash-dotted curve for $\Gamma_1/\Gamma_2 = 0.001$ and $J_y/\Gamma_2 = 100$, two of the three impurity-Majorana operators $\gamma_{x,y,z}$ are gapped out by the large J_y. We thus observe single-channel physics of the weaker channel, with coupling $\Gamma_1 = \Gamma_x$ in Eq. (85). Next, for $\Gamma_1 \ll J_y \ll \Gamma_2$ (blue dotted curve, $\Gamma_1/\Gamma_2 = 0.001$ and $J_y/\Gamma_2 = 0.1$), after approaching the single-channel value at $eV \simeq \Gamma_2$, the voltage dependence of the conductance reveals an antiresonance for $\Gamma_1 \lesssim eV \lesssim J_y$ with subsequent recovery at $eV \lesssim \Gamma_1$. Here, in the low-bias regime, a combined channel as in Eq. (85) is activated. Finally, for general nonzero couplings $\Gamma_{1,2}$ and J_y, we observe a complex interplay between the asymmetric two-channel Kondo effect and impurity hybridization phenomena. However, for our case with three coupled impurity-Majorana operators, the low-frequency transparency in Eq. (79) always approaches the unitary limit, $\mathcal{T}(\omega \to 0) = 1$. This behavior can be rationalized by noting that at sufficiently low energies, one (rotated) Majorana pair will effectively be gapped out for $J_y \neq 0$. The remaining third Majorana operator then remains free. This MZM provides a single-channel transport resonance pinned to the Fermi level, with the universal zero-bias conductance $G = e^2/2h$.

We conclude that the device in Fig. 1 allows for a complete solution of the nonequilibrium transport problem at the Toulouse point. An interesting open question for future research will be to address interaction corrections around this point, which can easily be included in the full counting statistics formalism used above [81,83].

VI. CONCLUDING REMARKS

In this paper, we have studied quantum transport through coupled Majorana box devices. Since Majorana boxes represent an attractive platform for realizing topological qubits, coupled box devices are of present interest for quantum information processing applications, see, e.g., Refs. [18,19]. When normal leads are tunnel coupled to such a system, the spin-1/2 degrees of freedom representing Majorana box qubits will be subject to Kondo screening via cotunneling processes, culminating in the topological Kondo effect [53]. Consequently, when different boxes are connected, one encounters competing Kondo effects and related phenomena in a non-Fermi-liquid setting.

For general systems of this type, we have introduced a powerful and versatile theoretical framework for studying the low-energy physics and quantum transport. Our theory employs Abelian bosonization of the lead fermions together with the Majorana-Klein fusion method of Refs. [54,55]. For a single box, the resulting problem is purely bosonic and admits an asymptotically exact solution for the corresponding non-Fermi-liquid fixed point [54,55]. However, for coupled-box systems, we found that additional local sets of Pauli operators due to nonconserved local fermion parities must be taken into account. Despite the complexity of the resulting problem, it is possible to make analytical progress. Approaching the physics both from the weak-coupling side (see our RG analysis in Sec. III) and in the strong-coupling regime (see our effective low-energy theory for the most relevant collective degrees of freedom in Sec. IV), a rich interplay between different types of single- or multibox topological Kondo effects has been encountered.

We have in detail examined the transport characteristics of the three perhaps most basic devices where nonconserved fermion parities play a central role. One of these includes the loop qubit device suggested in Ref. [19]. Importantly, the methods put forward in this paper also allow one to obtain nonperturbative transport results in moderately complex setups. This aspect should be especially valuable in view of the fact that transport measurements could give clear and unambiguous nonlocality signatures for Majorana states in such devices. At the fundamental level, nonsimple lead-MZM junctions cannot be described by purely 1D nonbranched networks that admit a solution in terms of the Majorana-Klein fusion approach, cf. Sec. II C. Therefore transport measurements in our setups may reveal more profound signatures of Majorana non-Abelian statistics when compared to the simple junction setups considered in experiments so far. While a detailed discussion of alternative non-Majorana transport scenarios, e.g., for the loop qubit device in Fig. 4, is beyond the scope of our paper, we hope that our predictions will soon be put to an experimental test.

ACKNOWLEDGMENTS

We thank A. Altland, F. Buccheri, K. Flensberg, L.A. Landau, C. Mora, E. Sela, and A. Zazunov for discussions. This work has been supported by the Deutsche Forschungsgemeinschaft within CRC TR 183 (project C01) and within Grant No. EG 96/11-1.

APPENDIX A: EXAMPLES FOR RG CONTRIBUTIONS

We here give further details and examples for the general RG equations in Sec. III A, which we illustrate for a device with four coupled Majorana boxes, see Fig. 8. We start with two examples for tunneling operators connecting leads in different subsectors and therefore involving Pauli strings. Our first example, with Pauli string length $n = 1$, comes from lowest-order tunneling events connecting a lead $j_a \in \mathcal{B}_a$ to lead l_a (resp. r_b) in Fig. 8, where the Pauli operator σ_x^1 (resp. σ_y^1) appears in Eq. (19). Note that lead l_a (resp. r_b) forms its own bosonic subsector, see Sec. III A. As the second example, again with $n = 1$, we could pick a tunneling path connecting some lead $j_a \in \mathcal{B}_a$ with a lead $k_b \in \mathcal{B}_b$ in Fig. 8. In that case, the Pauli operator σ_z^1 appears in Eq. (19).

Next, we discuss the cotunneling amplitudes $J_{jk}^{(\{\sigma\})}$ appearing in Eq. (20). Such amplitudes connect a lead $j = j_d \in \mathcal{B}_d$ in a bosonic subsector $\mathcal{B}_d$ to another lead $k = k_c \notin \mathcal{B}_d$ which is not part of this subsector, cf. Eq. (19). Here, lead k could be part of the bosonic subsector $\mathcal{B}_c$ in Fig. 8. For example, taking short tunneling paths connecting leads j_d and k_c in Fig. 8

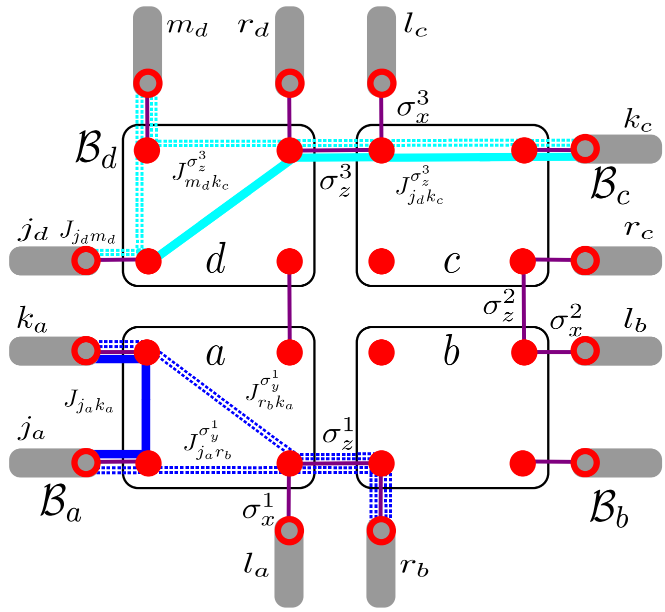

FIG. 8. Example for a coupled Majorana box device with four boxes (a,b,c,d), with symbols as in Figs. 1 and 2. The bosonic subsectors $\mathcal{B}_{a,b,c,d}$ contain $M_a = M_d = 2$ and $M_b = M_c = 1$ leads with simple lead-MZM contacts to the respective box. The device has four MZM-MZM tunnel bridges and three pairs of central leads $[(l_a,r_b),(l_b,r_c)$, and $(l_c,r_d)]$ with nonsimple lead-MZM contacts. Each central lead also forms its own subsector. Nonconserved local fermion parities are encoded by Pauli operators $\sigma_{x,y,z}^{m=1,2,3}$. We also illustrate how RG terms arise from contractions of cotunneling operators: (i) For $j_a \neq k_a \in \mathcal{B}_a$, the second term in Eq. (20) is due to contraction of $J_{j_a r_b}^{(\sigma_y^1)}$ and $J_{r_b k_a}^{(\sigma_y^1)}$ (dashed dark blue line) which renormalizes $J_{j_a k_a}$ (solid dark blue). (ii) For lead indices $j_d \neq m_d \in \mathcal{B}_d$, the contraction of $J_{j_d m_d}$ and $J_{m_d k_c}^{(\sigma_z^3)}$ (dashed cyan) renormalizes the amplitude $J_{j_d k_c}^{(\sigma_z^3)}$ (solid cyan), cf. Eq. (21).

(cyan lines), the Pauli string reduces to σ_z^3. Alternatively, lead k may correspond to a nonsimple lead-MZM contact. In Fig. 8, such leads are referred to as central leads. Such a lead forms a bosonic subsector $\mathcal{B}$ with $M = |\mathcal{B}| = 1$ by itself. For example, identifying lead $k = r_d$ (resp., $k = l_c$) in Fig. 8, the Pauli string reduces to the single Pauli operator σ_x^3 (resp., σ_y^3). In either case, pairs of cotunneling operators will only contribute to the RG flow of $J_{jk}^{(\{\sigma\})}$ if their contraction yields precisely the Pauli string $\sigma^1 \cdots \sigma^n$, see Fig. 8 (cyan lines).

The terms on the r.h.s. of Eq. (21) describe the renormalization of intersector cotunneling amplitudes with $j \in \mathcal{B}_1$ and $k \in \mathcal{B}_2$ due to the combination of an intersector tunneling with intrasector transitions in either sector $\mathcal{B}_{1,2}$. On top of this, one can have additional terms that involve intermediate excursions into different sectors $\mathcal{B} \neq \mathcal{B}_{1,2}$. Such terms have the schematic form

$$\frac{dJ_{jk}^{(\{\sigma\})}}{d\ell} \sim \sum_{m \notin (\mathcal{B}_1,\mathcal{B}_2)} J_{jm}^{(\{\sigma'\})} J_{mk}^{(\{\sigma''\})}, \tag{A1}$$

which contribute only if the contraction of both Pauli strings is consistent with $(\sigma^{1'} \cdots \sigma^{n'})(\sigma^{1''} \cdots \sigma^{n''}) \sim \sigma^1 \cdots \sigma^n$. An example for such a process is shown in Fig. 9 using the same system as in Fig. 8. The contracted Pauli strings here share two

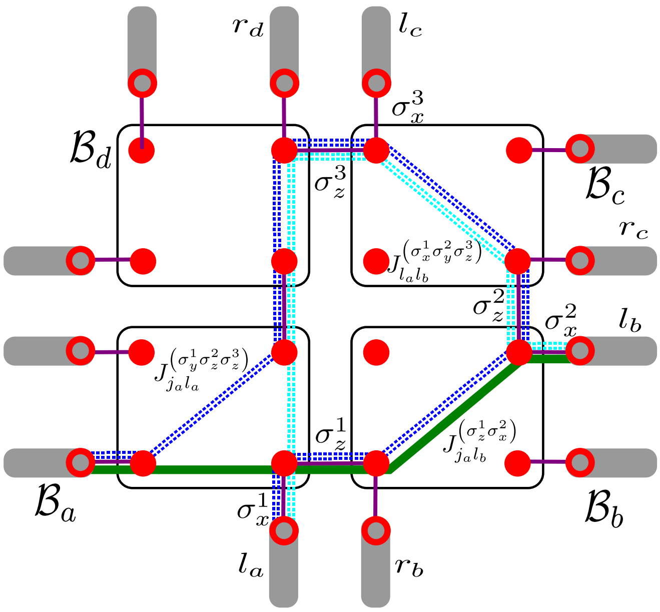

FIG. 9. Illustration of additional contributions to the RG flow of cotunneling amplitudes connecting lead $j_a \in \mathcal{B}_a$ and lead l_b beyond those specified in Eq. (21), using the same device as in Fig. 8. By contracting the two cotunneling operators with amplitudes $J_{j_a l_a}^{(\sigma_y^1\sigma_z^2\sigma_z^3)}$ (dashed dark blue) and $J_{l_a l_b}^{(\sigma_x^1\sigma_y^2\sigma_z^3)}$ (dashed cyan), the composite Pauli string is given by $(\sigma_y^1\sigma_z^2\sigma_z^3)(\sigma_x^1\sigma_y^2\sigma_z^3) \sim \sigma_z^1\sigma_x^2$. This contraction contributes to the RG flow of $J_{j_a l_b}^{(\sigma_z^1\sigma_x^2)}$ (green solid).

overlapping anticommuting Pauli operators and hence overall are commuting.

APPENDIX B: RG FLOW FOR THE TWO-BOX EXAMPLE

We here discuss the isotropization of equivalent couplings for the two-box device with $M_L = 3$ and $M_R = 2$ in Fig. 3, see Sec. III B, where equivalence is meant with respect to the Pauli operator content. In order to check whether the system exhibits isotropization, we perform a numerical integration of the RG equations and test how anisotropies present in the bare (initial) couplings develop during the RG flow, cf. Ref. [63]. Using the couplings in Eqs. (27) and (28), we define average couplings

$$\begin{aligned} J_L &= \frac{1}{M_L(M_L-1)} \sum_{j\neq k\in\mathcal{B}_L} (J_L)_{jk}, \\ J_{X,l} &= \frac{1}{M_L} \sum_{k\in\mathcal{B}_L} (J_X)_{lk}, \\ J_{Y,r} &= \frac{1}{M_L} \sum_{k\in\mathcal{B}_L} (J_Y)_{rk}, \\ J_Z &= \frac{1}{M_L M_R} \sum_{j\in\mathcal{B}_L, k\in\mathcal{B}_R} (J_Z)_{jk}, \end{aligned} \tag{B1}$$

and similarly for J_R, $J_{X,r}$, and $J_{Y,l}$. We then monitor the anisotropy measures, $\Sigma_x(\ell)$, for all seven coupling families (indexed by x), see Sec. III B. These measures are defined from

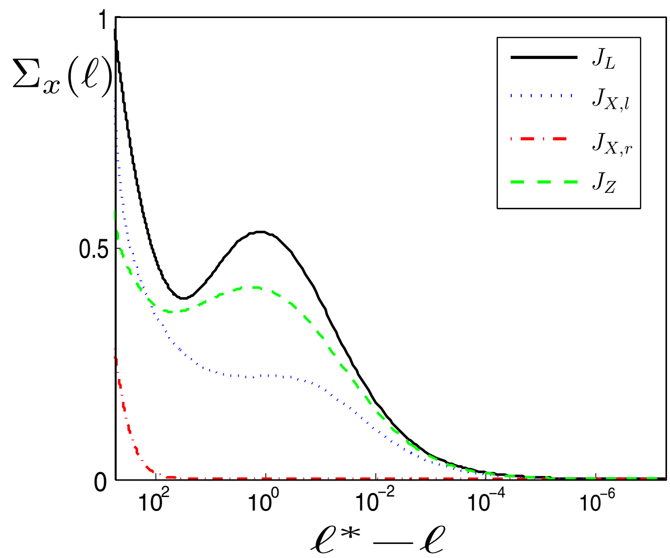

FIG. 10. RG flow of the anisotropy measures Σ_x, cf. Eq. (B2), for different coupling families x in the two-box device of Fig. 3. The weak-coupling RG approach breaks down at $\ell = \ell^*$, where couplings start to diverge. We show Σ_x vs $\ell^* - \ell$ on a logarithmic scale. All coupling families become isotropic during the RG flow.

the standard deviation of the coupling family normalized by the respective average value in Eq. (B1), see also [63],

$$\Sigma_{J_L}^2 = \frac{1}{M_L(M_L-1)} \sum_{j,k\in\mathcal{B}_L, j\neq k} \frac{[(J_L)_{jk} - J_L]^2}{J_L^2}, \tag{B2}$$

and likewise for the other coupling families. Figure 10 shows the results of a numerical solution of the RG equations (29)–(31) with a random choice for the initial couplings, cf. Ref. [63]. We have checked that the qualitative behavior seen in Fig. 10 is largely insensitive to the chosen random realization. Figure 10 shows that all anisotropies become gradually suppressed during the RG flow, which implies effectively isotropic behavior within each coupling family and thereby justifies Eq. (32).

APPENDIX C: BIASED LEADS IN SIMPLY-COUPLED MAJORANA BOXES

We here relate our results for the biased two-box setting in Sec. V with those of Béri [67], see also Fig. 6. We first note that for a decoupled central lead in Fig. 1, in equilibrium we should recover a single-impurity TKE of the combined island with $M = M_L + M_R$ leads. The distinction into different boxes then becomes obsolete. Since Pauli strings are not involved anymore, there is no *a priori* reason for a specific partitioning of leads into subsectors. However, such a splitting follows from the applied bias voltages in a transport measurement, where leads in two subsectors $\mathcal{B}_{a,b}$ are biased relative to each other. In Sec. V, we have considered the case $M_{a,b} = M_{L,R} = 2$, while Béri [67] investigated the case of just one biased lead ($M_a = 1$) in an otherwise equilibrium M-terminal TKE, $M_b = M - 1$. We next recall the strong-coupling Hamiltonian for this system, see Sec. IV A,

$$H_{ab} = -J\cos(g_a\Phi_a - g_b\Phi_b) = -J\cos(g\Phi), \tag{C1}$$

with the collective intersector coupling J and the center-of-mass phase fields $\Phi_{a,b}$, cf. Eq. (41), for leads in subsectors $\mathcal{B}_{a,b}$, where $g_{a,b} = 1/\sqrt{M_{a,b}}$. Equation (C1) defines the linear combination Φ with $g = \sqrt{g_a^2 + g_b^2}$.

We can now obtain exact nonequilibrium results for charge transport between $\mathcal{B}_{a,b}$ by following the steps in Ref. [67]. To arrive at a backscattering model from Eq. (C1), one first expresses $\Phi = (\Phi_L + \Phi_R)/\sqrt{2}$ in terms of left- and right-moving chiral boson fields $\phi_{L/R}$. One can then define the backscattering interaction $g_{\rm bs} = g^2/2$ [67], where Eq. (C1) gives $H_{ab} = -J\cos[\sqrt{g_{\rm bs}}(\Phi_L + \Phi_R)]$. The fractional charge e^* governing elementary charge transfer processes between subsectors in this non-Fermi-liquid system is given by the ratio [67]

$$\frac{e^*}{e} = \frac{1}{g_{\rm bs}} = \frac{2M_aM_b}{M_a + M_b}. \tag{C2}$$

In particular, for $M_a = 1$ and $M_b = M - 1$, Eq. (C2) yields the TKE result for a single biased lead, $e^*_{\rm TKE} = 2e(M-1)/M$, see Refs. [56,67]. For the symmetric case $M_a = M_b = M/2$, Eq. (C2) instead gives $e^* = eM/2$. For instance, putting $M = 2$, we confirm that transport is due to cotunneling of electrons [45–47]. In our two-box setup with $M = 4$, Eq. (C2) instead gives $e^*_{LR} = 2e$. Transport between the left and right side is thus mediated by the cross-correlated Andreev reflection (AR) of Cooper pairs, cf. Fig. 6, where one expects the conductance $G_{LR} = 2e^2/h$. However, in Sec. V A, we found that a two-terminal conductance measurement between a pair of *individual* leads $j \in \mathcal{B}_L$ and $k \in \mathcal{B}_R$ will give the two-channel Kondo value $G_{jk} = e^2/2h$. The conductance G_{LR} instead follows by summing over all participating leads, $G_{LR} = \sum_{j,k} G_{jk} = 2e^2/h$, representing a collective intersector conductance measurement.

As illustrated in Fig. 6, one can further reconcile the physics encoded by e^* in Eq. (C2) with previous work on the TKE [54–56,67]. A correlated AR process comprises an AR at one lead (absorbing charge $2e$) along with the equal-probability emission of charge $2e/M$ into all M leads, without net charge accumulation on the island. For a single biased lead, this yields $e^*_{\rm TKE}$ above. Next we note that between leads in a biased subsector $\mathcal{B}_a$, charge dipoles are forbidden by strong intrasector couplings. In order to return to an allowed configuration, a total of M_a correlated AR events (one from each lead in $\mathcal{B}_a$) have to participate in transport. Counting after this sequence, each lead in $\mathcal{B}_a$ has emitted charge

$$q_a = 2e\left[\frac{M-1}{M} - (M_a - 1)\frac{1}{M}\right] = 2e\frac{M_b}{M}, \tag{C3}$$

with $M - M_a = M_b$. Similarly, we have $q_b = -2eM_a/M$ absorbed charges per lead in $\mathcal{B}_b$, due to M_a split Cooper pairs. The total, collective charge transported by an effective low-energy process between the two subsectors then is $e^* = M_a|q_a| = M_b|q_b|$, as reported in Eq. (C2).

From the viewpoint of two-terminal transport between individual leads $j \in \mathcal{B}_a$ and $k \in \mathcal{B}_b$, cf. Sec. V, the total outgoing (incoming) charge is democratically distributed into (gathered from) all leads in the opposite sector. Therefore only the effective charge $e^*_{jk} = q_a/M_b = -q_b/M_a = 2e/M$ is transferred directly from lead j to k. Again summing over leads in the subsectors, one recovers $e^* = \sum_{j,k} e^*_{jk}$. For our $M = 4$ case at hand, in two-terminal transport we reproduce the two-channel Kondo result in Sec. V A, $e^*_{jk} = e/2$, while collective intersector transport involves Cooper pairs with $e^*_{LR} = 2e$ in Eq. (C2).

[1] J. Alicea, Rep. Prog. Phys. **75**, 076501 (2012).
[2] M. Leijnse and K. Flensberg, Semicond. Sci. Techn. **27**, 124003 (2012).
[3] C. W. J. Beenakker, Annu. Rev. Con. Mat. Phys. **4**, 113 (2013).
[4] R. Aguado, Riv. Nuovo Cimento **40**, 523 (2017).
[5] R. M. Lutchyn, E. P. A. M. Bakkers, L. P. Kouwenhoven, P. Krogstrup, C. M. Marcus, and Y. Oreg, arXiv:1707.04899.
[6] A. Yu. Kitaev, Usp. Fiz. Nauk (Suppl) **171**, 131 (2001).
[7] J. D. Sau, S. Tewari, and S. Das Sarma, Phys. Rev. A **82**, 052322 (2010).
[8] J. Alicea, Y. Oreg, G. Refael, F. von Oppen, and M. P. A. Fisher, Nat. Phys. **7**, 412 (2011).
[9] B. M. Terhal, F. Hassler, and D. P. DiVincenzo, Phys. Rev. Lett. **108**, 260504 (2012).
[10] T. Hyart, B. van Heck, I. C. Fulga, M. Burrello, A. R. Akhmerov, and C. W. J. Beenakker, Phys. Rev. B **88**, 035121 (2013).
[11] S. Das Sarma, M. Freedman, and C. Nayak, npj Quantum Information **1**, 15001 (2015).
[12] S. Vijay, T. H. Hsieh, and L. Fu, Phys. Rev. X **5**, 041038 (2015).
[13] L. A. Landau, S. Plugge, E. Sela, A. Altland, S. M. Albrecht, and R. Egger, Phys. Rev. Lett. **116**, 050501 (2016).
[14] S. Plugge, L. A. Landau, E. Sela, A. Altland, K. Flensberg, and R. Egger, Phys. Rev. B **94**, 174514 (2016).
[15] D. Aasen, M. Hell, R. V. Mishmash, A. Higginbotham, J. Danon, M. Leijnse, T. S. Jespersen, J. A. Folk, C. M. Marcus, K. Flensberg, and J. Alicea, Phys. Rev. X **6**, 031016 (2016).
[16] S. Vijay and L. Fu, Phys. Rev. B **94**, 235446 (2016).
[17] J. Manousakis, A. Altland, D. Bagrets, R. Egger, and Y. Ando, Phys. Rev. B **95**, 165424 (2017).
[18] S. Plugge, A. Rasmussen, R. Egger, and K. Flensberg, New J. Phys. **19**, 012001 (2017).
[19] T. Karzig, C. Knapp, R. M. Lutchyn, P. Bonderson, M. B. Hastings, C. Nayak, J. Alicea, K. Flensberg, S. Plugge, Y. Oreg, C. M. Marcus, and M. H. Freedman, Phys. Rev. B **95**, 235305 (2017).
[20] D. Litinski, M. S. Kesselring, J. Eisert, and F. von Oppen, Phys. Rev. X **7**, 031048 (2017).
[21] D. Litinski and F. von Oppen, Phys. Rev. B **97**, 205404 (2018).
[22] V. Mourik, K. Zuo, S. M. Frolov, S. R. Plissard, E. P. A. Bakkers, and L. P. Kouwenhoven, Science **336**, 1003 (2012).
[23] M. T. Deng, C. L. Yu, G. Y. Huang, M. Larsson, P. Caroff, and H. Q. Xu, Nano Lett. **12**, 6414 (2012).
[24] A. Das, Y. Ronen, Y. Most, Y. Oreg, M. Heiblum, and H. Shtrikman, Nat. Phys. **8**, 887 (2012).
[25] L. P. Rokhinson, X. Liu, and J. K. Furdyna, Nat. Phys. **8**, 795 (2012).

[26] W. Chang, S. M. Albrecht, T. S. Jespersen, F. Kuemmeth, P. Krogstrup, J. Nygård, and C. M. Marcus, Nat. Nanotechnol. **10**, 232 (2015).
[27] P. Krogstrup, N. L. B. Ziino, W. Chang, S. M. Albrecht, M. H. Madsen, E. Johnson, J. Nygård, C. M. Marcus, and T. S. Jespersen, Nat. Mater. **14**, 400 (2015).
[28] A. P. Higginbotham, S. M. Albrecht, G. Kirsanskas, W. Chang, F. Kuemmeth, T. S. Jespersen, J. Nygård, K. Flensberg, and C. M. Marcus, Nat. Phys. **11**, 1017 (2015).
[29] S. M. Albrecht, A. P. Higginbotham, M. Madsen, F. Kuemmeth, T. S. Jespersen, J. Nygård, P. Krogstrup, and C. M. Marcus, Nature (London) **531**, 206 (2016).
[30] M. T. Deng, S. Vaitiekenas, E. B. Hansen, J. Danon, M. Leijnse, K. Flensberg, J. Nygård, P. Krogstrup, and C. M. Marcus, Science **354**, 1557 (2016).
[31] Ö. Gül, H. Zhang, F. K. de Vries, J. van Veen, K. Zuo, V. Mourik, S. Conesa-Boj, M. P. Nowak, D. J. van Woerkom, M. Quintero-Pérez, M. C. Cassidy, A. Geresdi, S. Koelling, D. Car, S. R. Plissard, E. P. A. M. Bakkers, and L. P. Kouwenhoven, Nano Lett. **17**, 2690 (2017).
[32] H. Zhang, Ö. Gül, S. Conesa-Boj, M. Nowak, M. Wimmer, K. Zuo, V. Mourik, F. K. de Vries, J. van Veen, M. W. A. de Moor, J. D. S. Bommer, D. J. van Woerkom, D. Car, S. R. Plissard, E. P. A. M. Bakkers, M. Quintero-Perez, M. C. Cassidy, S. Koelling, S. Goswami, K. Watanabe, T. Taniguchi, and L. P. Kouwenhoven, Nat. Commun. **8**, 16025 (2017).
[33] S. M. Albrecht, E. B. Hansen, A. P. Higginbotham, F. Kuemmeth, T. S. Jespersen, J. Nygård, P. Krogstrup, J. Danon, K. Flensberg, and C. M. Marcus, Phys. Rev. Lett. **118**, 137701 (2017).
[34] F. Nichele, A. C. C. Drachmann, A. M. Whiticar, E. C. T. O'Farrell, H. J. Suominen, A. Fornieri, T. Wang, G. C. Gardner, C. Thomas, A. T. Hatke, P. Krogstrup, M. J. Manfra, K. Flensberg, and C. M. Marcus, Phys. Rev. Lett. **119**, 136803 (2017).
[35] H. J. Suominen, M. Kjaergaard, A. R. Hamilton, J. Shabani, C. J. Palmstrøm, C. M. Marcus, and F. Nichele, Phys. Rev. Lett. **119**, 176805 (2017).
[36] S. Gazibegovich, D. Car, H. Zhang, S. C. Balk, J. A. Logan, M. W. A. de Moor, M. C. Cassidy, R. Schmits, D. Xu, G. Wang, P. Krogstrup, R. L. M. Op het Veld, J. Shen, D. Bouman, B. Shojaei, D. Pennachio, J. S. Lee, P. J. van Veldhoven, S. Koelling, M. A. Verheijen, L. P. Kouwenhoven, C. J. Palmstrøm, and E. P. A. M. Bakkers, Nature (London) **548**, 434 (2017).
[37] H. Zhang, C. X. Liu, S. Gazibegovic, D. Xu, J. A. Logan, G. Wang, N. van Loo, J. D. S. Bommer, M. W. A. de Moor, D. Car, R. L. M. Op het Veld, P. J. van Veldhoven, S. Koelling, M. A. Verheijen, M. Pendharkar, D. J. Pennachio, B. Shojaei, J. S. Lee, C. J. Palmstrom, E. P. A. M. Bakkers, S. Das Sarma, and L. P. Kouwenhoven, Nature (London) **556**, 74 (2018).
[38] M. T. Deng, S. Vaitiekénas, E. Prada, P. San-Jose, J. Nygård, P. Krogstrup, R. Aguado, and C. M. Marcus, arXiv:1712.03536.
[39] D. Laroche, D. Bouman, D. J. van Woerkom, A. Proutski, C. Murthy, D. I. Pikulin, C. Nayak, R. J. J. van Gulik, J. Nygård, P. Krogstrup, L. P. Kouwenhoven, and A. Geresdi, arXiv:1712.08459.
[40] S. Nadj-Perge, I. K. Drozdov, J. Li, H. Chen, S. Jeon, J. Seo, A. H. MacDonald, B. A. Bernevig, and A. Yazdani, Science **346**, 602 (2014).
[41] M. Ruby, F. Pientka, Y. Peng, F. von Oppen, B. W. Heinrich, and K. J. Franke, Phys. Rev. Lett. **115**, 197204 (2015).
[42] H. H. Sun, K. W. Zhang, L. H. Hu, C. Li, G. Y. Wang, H. Y. Ma, Z. A. Xu, C. L. Gao, D. D. Guan, Y. Y. Li, C. Liu, D. Qian, Y. Zhou, L. Fu, S. C. Li, F. C. Zhang, and J. F. Jia, Phys. Rev. Lett. **116**, 257003 (2016).
[43] B. E. Feldman, M. T. Randeria, J. Li, S. Jeon, Y. Xie, Z. Wang, I. K. Drozdov, B. Andrei Bernevig, and A. Yazdani, Nat. Phys. **13**, 286 (2017).
[44] R. S. Deacon, J. Wiedenmann, E. Bocquillon, F. Domínguez, T. M. Klapwijk, P. Leubner, C. Brüne, E. M. Hankiewicz, S. Tarucha, K. Ishibashi, H. Buhmann, and L. W. Molenkamp, Phys. Rev. X **7**, 021011 (2017).
[45] L. Fu, Phys. Rev. Lett. **104**, 056402 (2010).
[46] A. Zazunov, A. L. Yeyati, and R. Egger, Phys. Rev. B **84**, 165440 (2011).
[47] R. Hützen, A. Zazunov, B. Braunecker, A. L. Yeyati, and R. Egger, Phys. Rev. Lett. **109**, 166403 (2012).
[48] S. Plugge, A. Zazunov, P. Sodano, and R. Egger, Phys. Rev. B **91**, 214507 (2015).
[49] C. Xu and L. Fu, Phys. Rev. B **81**, 134435 (2010).
[50] Z. Nussinov, G. Ortiz, and E. Cobanera, Phys. Rev. B **86**, 085415 (2012).
[51] A. Roy, B. M. Terhal, and F. Hassler, Phys. Rev. Lett. **119**, 180508 (2017).
[52] K. Snizhko, R. Egger, and Y. Gefen, Phys. Rev. B **97**, 081405(R) (2018).
[53] B. Béri and N. R. Cooper, Phys. Rev. Lett. **109**, 156803 (2012).
[54] A. Altland and R. Egger, Phys. Rev. Lett. **110**, 196401 (2013).
[55] B. Béri, Phys. Rev. Lett. **110**, 216803 (2013).
[56] A. Zazunov, A. Altland, and R. Egger, New J. Phys. **16**, 015010 (2014).
[57] A. Altland, B. Béri, R. Egger, and A. M. Tsvelik, Phys. Rev. Lett. **113**, 076401 (2014).
[58] E. Eriksson, C. Mora, A. Zazunov, and R. Egger, Phys. Rev. Lett. **113**, 076404 (2014).
[59] M. R. Galpin, A. K. Mitchell, J. Temaismithi, D. E. Logan, B. Béri, and N. R. Cooper, Phys. Rev. B **89**, 045143 (2014).
[60] E. Eriksson, A. Nava, C. Mora, and R. Egger, Phys. Rev. B **90**, 245417 (2014).
[61] O. Kashuba and C. Timm, Phys. Rev. Lett. **114**, 116801 (2015).
[62] F. Buccheri, H. Babujian, V. E. Korepin, P. Sodano, and A. Trombettoni, Nucl. Phys. B **896**, 52 (2015).
[63] S. Plugge, A. Zazunov, E. Eriksson, A. M. Tsvelik, and R. Egger, Phys. Rev. B **93**, 104524 (2016).
[64] L. Herviou, K. Le Hur, and C. Mora, Phys. Rev. B **94**, 235102 (2016).
[65] A. Zazunov, F. Buccheri, P. Sodano, and R. Egger, Phys. Rev. Lett. **118**, 057001 (2017).
[66] Z. Q. Bao and F. Zhang, Phys. Rev. Lett. **119**, 187701 (2017).
[67] B. Béri, Phys. Rev. Lett. **119**, 027701 (2017).
[68] L. A. Landau and E. Sela, Phys. Rev. B **95**, 035135 (2017).
[69] K. Michaeli, L. A. Landau, E. Sela, and L. Fu, Phys. Rev. B **96**, 205403 (2017).
[70] A. O. Gogolin, A. A. Nersesyan, and A. M. Tsvelik, *Bosonization and Strongly Correlated Systems* (Cambridge University Press, Cambridge, UK, 1998).
[71] A. Altland and B. Simons, *Condensed Matter Field Theory*, 2nd ed. (Cambridge University Press, Cambridge, UK, 2010).
[72] C. Nayak, M. P. A. Fisher, A. W. W. Ludwig, and H. H. Lin, Phys. Rev. B **59**, 15694 (1999).

[73] M. Oshikawa, C. Chamon, and I. Affleck, J. Stat. Mech. (2006) P02008.
[74] H. Yi and C. L. Kane, Phys. Rev. B **57**, R5579(R) (1998).
[75] H. Yi, Phys. Rev. B **65**, 195101 (2002).
[76] C. Jayaprakash, H. R. Krishna-murthy, and J. W. Wilkins, Phys. Rev. Lett. **47**, 737 (1981).
[77] B. A. Jones, C. M. Varma, and J. W. Wilkins, Phys. Rev. Lett. **61**, 125 (1988).
[78] I. Affleck, A. W. W. Ludwig, and B. A. Jones, Phys. Rev. B **52**, 9528 (1995).
[79] V. J. Emery and S. Kivelson, Phys. Rev. B **46**, 10812 (1992).
[80] M. Fabrizio, A. O. Gogolin, and Ph. Nozières, Phys. Rev. B **51**, 16088 (1995).
[81] A. O. Gogolin and A. Komnik, Phys. Rev. B **73**, 195301 (2006).
[82] A. K. Mitchell, L. A. Landau, L. Fritz, and E. Sela, Phys. Rev. Lett. **116**, 157202 (2016).
[83] L. A. Landau, E. Cornfeld, and E. Sela, Phys. Rev. Lett. **120**, 186801 (2018).
[84] I. Affleck and D. Giuliano, J. Stat. Mech. (2013) P06011.
[85] R. Egger and A. Komnik, Phys. Rev. B **57**, 10620 (1998).